Author/s:
Siu, PH;Karoly, PJ;Mansour L., S;Soto-Breceda, A;Kuhlmann, L;Cook, MJ;Grayden, DB

Title:
Structural Eigenmodes of the Brain to Improve the Source Localization of EEG: Application to Epileptiform Activity

Date:
2026

Citation:
Siu, P. H., Karoly, P. J., Mansour L., S., Soto-Breceda, A., Kuhlmann, L., Cook, M. J. & Grayden, D. B. (2026). Structural Eigenmodes of the Brain to Improve the Source Localization of EEG: Application to Epileptiform Activity. Advanced Science, 13, pp.1-19. https://doi.org/10.1002/advs.202516802.

Persistent Link:
https://hdl.handle.net/11343/369104

Advanced Science

ADVANCED SCIENCE Open Access

www.advancedscience.com

RESEARCH ARTICLE OPEN ACCESS

Structural Eigenmodes of the Brain to Improve the Source Localization of EEG: Application to Epileptiform Activity

Pok Him Siu[1,2] | Philippa J. Karoly[1,2] | Sina Mansour L.[1,3] | Artemio Soto-Breceda[4] | Levin Kuhlmann[5] | Mark J. Cook[1,2,6] | David B. Grayden[1,2,6]

[1]Department of Biomedical Engineering, The University of Melbourne, Melbourne, Australia | [2]Graeme Clark Institute, The University of Melbourne, Melbourne, Australia | [3]National University of Singapore, Singapore, Singapore | [4]Grenoble Institut des Neurosciences, INSERM, Grenoble (La Tronche), France | [5]Department of Data Science & AI, Monash University, Melbourne, Australia | [6]Department of Medicine, St Vincent's Hospital, Melbourne, The University of Melbourne, Melbourne, Australia

Correspondence: Pok Him Siu (pokhim.siu@student.unimelb.edu.au)

Received: 1 September 2025 | **Revised:** 3 March 2026 | **Accepted:** 12 March 2026

Keywords: connectome | EEG | epilepsy | geometric eigenmodes | source localization

ABSTRACT

A fundamental view of neuroscience is that, in addition to neuronal activity, the structure of the brain constrains and explains brain function. An alluring formalism in computational neuroscience has been the generation of structural eigenmodes of neural activity from a matrix representing the anatomy of the brain. Traditionally, brain connectomics has been the gold standard for the coupling between structure and function. However, it has recently been suggested that simpler brain geometry can provide more explanatory power in fMRI. An adjacent modality is the source localization problem of EEG, which aims to identify the underlying generators of EEG recordings. The underdetermined nature of the problem requires sufficient constraints to produce realistic and unique solutions of source activity. In this work, a simple framework for incorporating different forms of structural brain eigenmodes to constrain the source localization problem in epilepsy is presented. Geometric eigenmodes were found to be able to reconstruct the spread of a seizure through the brain slightly better than connectome eigenmodes, and both types of structural modes significantly outperformed commonly used approaches.

1 | Introduction

Epilepsy is estimated to affect around 0.6% of the global population [1]. Of these estimated 50 million cases of epilepsy, around 30% are antiepileptic drug-resistant [1]. In 50% of the latter cases, the patient is diagnosed with focal epilepsy [2], where, for a carefully selected subset of patients, the treatment is to resect the culpable region of the brain, known as the epileptogenic zone. Accurate identification of the epileptogenic zone is pivotal to the diagnosis, treatment, and outcomes for these patients. The current state of the art involves patients undergoing multiday invasive studies to determine the epileptogenic zone [2]. However, methods such as stereo-electroencephalography (sEEG) are limited in their spatial coverage, come with significant risks and discomfort, and require a clear pre-implantation hypothesis [3].

Electroencephalography (EEG) and magnetoencephalography (MEG) are foundational tools in neuroscience for analysing the state of the brain non-invasively. The key advantage of these macroscopic, electrophysiological recordings are their high temporal resolution, but the trade-off is the relatively low spatial resolution of their direct measurements. A core property of EEG/MEG is that these signals are a weighted sum of neural activity and, by themselves, cannot directly define the underlying sources of neural activity.

Source imaging is a mathematical technique that aims to recreate the activity of the underlying neural sources from EEG/MEG data. However, this transformation typically involves a lower number of electrodes ($\sim 10^2$) being mapped to a notably larger number of neural sources ($\sim 10^3$–10^4) and, therefore, is an underdetermined mathematical problem. The underdetermined nature of the source imaging problem requires sufficient constraints to produce realistic and unique solutions of source activity [4, 5]. Source imaging algorithms are hence reliant on two core components: i) a realistic volume conduction model that solves Maxwell's equations to convert from source space to sensor space (the 'forward problem') [6] and ii) mathematical constraints to provide a unique solution to the inverse transformation from sensor space to source space. Current algorithms employ biological realism with the forward model. However, the inversion constraints are typically less motivated by physiology and more by mathematical and statistical arguments [5, 7]. For instance, the minimum-norm constraint provides the lowest-energy solution, which is a plausible but not necessarily accurate approximation of neural behavior. Constraints on the smoothness and focality of sources are also common and, although both can be said to be loosely motivated by neurophysiology, both also have a tendency to deliver biologically implausible results in practice [8].

A recent study proposed that the geometry of the brain offers a fundamental but simplistic constraint on dynamic neural activity [9]. The construction of geometric eigenmodes of the brain's physical shape was found to offer a biologically plausible explanation of associated excitation between brain regions. Since that seminal paper, geometric eigenmodes have found varied applications in neuroscience, such as analysing the psychological effects of meditation [10], quantifying hemispheric asymmetry [11], and fingerprinting the brain to assess adolescent mental health [12]. Just as the Fourier transform decomposes complex temporal signals into a set of orthogonal sine and cosine functions, geometric eigenmodes of the brain form a spatial basis that can be used to represent distributed patterns of neural activity. Each eigenmode reflects a standing wave pattern constrained by the geometry of the brain, enabling efficient reconstruction and analysis of large-scale brain dynamics. Having such a clean modal decomposition enables geometric eigenmodes to offer a new means to constrain the source localization problem of EEG and MEG based on our current understanding of the brain's structure and function.

The geometry of the brain is not the only sensible structure to create these structural eigenmodes. Connectome eigenmodes, based on a matrix representation of the anatomical connectivity of the brain, may offer even more utility given that these account for both short-range local connections, as well as long-range white matter tractography. Connectome eigenmodes have a longer history and have advanced our understanding of structure-function coupling in several contexts, including gradients of behavioral specialization [13] and epilepsy [14]. Early studies suggested that the explanatory power of geometric eigenmodes exceeded structural connectomes for explaining spontaneous and task-evoked conditions in fMRI data [9]. However, several subsequent studies have provided conflicting evidence that connectome eigenmodes are similar or superior to geometric eigenmodes [15, 16]. Adjacent to these structural eigenmodes, functional eigenmodes constructed on observed neural activity have had remarked success in characterizing network dynamics and in epilepsy [17, 18]. Given the utility of eigenmodes to analyze neuroimaging data, and recent preliminary applications of eigenmode-based constraints in source localization [19–21], incorporating either a geometric or connectome eigenmode decomposition could improve the tractability of the inversion step in source imaging algorithms, but it is unclear which would be superior.

To understand the distinction between geometric and connectome approaches, validating novel source imaging algorithms requires a reliable source of truth; i.e., a dataset where both EEG/MEG are recorded alongside known neural sources. In practice, this ground truth is rarely available, and source imaging studies typically rely on simulated datasets or studies where the true source can be assumed from behavioral manifestations (such as the onset zone of epileptic seizures or evoked responses to stimuli). There are now two compelling reasons for creating a realistic simulation as a test data set. First, a sufficiently complex simulation enables the differentiation between geometric and connectome eigenmodes in terms of their expressiveness. Second, for the problem of source localization in epilepsy, the underlying sources within the epileptic zone cannot be directly experimentally verified. Currently, the best measure of success is a binary classification of whether resective surgery was effective in stopping or reducing seizures [22, 23]. By introducing a realistic simulation of the underlying sources of epileptic activity with its corresponding EEG activity, a test set with a known ground truth can be used to understand the differences between different source localization methodologies and conditions. Previous studies have typically focused on one to a few sources of various spatial [21, 24–28], but such sources are biologically questionable given that the brain is known to be a highly interconnected and complex hierarchical structure [29–31] that is capable of producing rhythmic and wavelike activity with wavelengths spanning several centimetres [9, 32, 33]. Building on successes in computational neuroscience [17, 34–36], we constructed dynamical neural mass models to produce realistic simulations of seizures.

In this study, we evaluated the utility of geometric and connectome eigenmodes as basis functions for constraining the problem of EEG source localization. In doing so, we aimed to explore the following research questions:

1. Do geometric and connectome eigenmodes differ in their capacity to reflect neurologically meaningful activity?
2. Can incorporating such structural modes into inverse models enhance the efficiency and accuracy of electrophysiological source localization?
3. Does structural eigenmode source localization show potential for improving the localization of epileptogenic zones in patients with epilepsy?

2 | Methods

The Methods section first describes the creation of geometric and connectome eigenmodes using real-world structural brain data, and then explains how structural eigenmodes were integrated into a source localization method. The following sections then

outline the validation datasets and evaluation metrics deployed to test the eigenmode-constrained source imaging approach.

2.1 | Structural Brain Data

Structural connectivity data from the Human Connectome Project (HCP) [37] was used, with HCP Subject 100206 (HCP100206) as the primary subject used in this work. The T1 MRI image with skull included was used to generate surface meshes in the subject's native space for the skin, skull, and cortex using Freesurfer's recon-all [38]. The cortical mesh from fsaverage template space was also used to test the effects of using group-averaged structural data in the source imaging pipeline. The individual subject's cortical mesh was aligned to the fsaverage template mesh, which consisted of 163,842 vertices per hemisphere.

Each vertex was attributed to one of the 1000 cortical regions of the Yan-1000 homotopic cortical parcellation atlas [39]. The location of each cortical region was defined as the centroid of its vertex coordinates. In addition to the 1000 cortical regions, 19 subcortical structures, defined by the cifti grayordinate template [40], were also included, resulting in a 1019-region parcellation of the entire brain.

The individual's structural connectome was computed using a diffusion MRI tractography pipeline detailed elsewhere [41, 42] using MRtrix3 software [43]. In summary, fibre orientation distributions (FODs) were computed from tissue-specific response functions via Multi-Shell Multi-Tissue Constrained Spherical Deconvolution [44, 45]. A total of five million tractography streamlines were estimated by an anatomically constrained probabilistic tractography algorithm based on second-order integration over FODs [46, 47]. Notably, streamlines were randomly seeded from the gray matter-white matter interface. A radial search with a maximum radius threshold of 4 mm was used to map streamlines to the regional parcellation, resulting in a 1019x1019 connectivity matrix of streamline counts. The matrix of streamline counts was then normalized by the maximum streamline count to end in a normalized connectivity matrix with entries between 0 and 1. In addition, a 1019x1019 streamline length matrix was computed to quantify average streamline lengths between all pairs of connected regions. To obtain the group-averaged connectivity matrix of streamline counts, the sum of streamlines between regions was taken for each patient, and the aggregate matrix normalized between 0 and 1.

2.2 | Eigenmode Creation

2.2.1 | Geometric Eigenmodes

Geometric eigenmodes (Figure 1a) were constructed by solving the eigenvalue problem with the Laplace-Beltrami operator on the surface mesh of the brain [9],

$$\nabla^2\psi = \Delta\psi = -\lambda\psi \tag{1}$$

where ∇ is the gradient operator, Δ is the Laplace-Beltrami operator, and ψ represents the set of geometric eigenmodes with their corresponding eigenvalues λ. These eigenvalues and eigenmodes were ordered according to increasing spatial frequency such that ψ_1 was the eigenmode with the longest wavelength. Geometric eigenmodes were also grouped into distinct eigengroups of similar wavelengths of size $2\ell + 1$, where ℓ is the ℓ-th eigengroup. The geometric eigenmodes were originally constructed on the 10 242 vertices white-matter surface mesh per hemisphere (icosahedron 5 spacing), and then, reduced to a 1000 region source space by averaging all vertices within each brain region of the Yan-1000 brain region parcellation [39] to match the spatial resolution of the connectome. The full set of geometric eigenmodes for the whole cortex was then the concatenation of the eigenmodes constructed for each hemisphere.

2.2.2 | Connectome Eigenmodes

Connectome eigenmodes (Figure 1b) were constructed by solving the eigenvalue problem on the graph Laplacian representation of the connectome [13],

$$L'\psi = -\lambda\psi \tag{2}$$

where L' is the normalized graph Laplacian, a discrete version of the Laplace-Beltrami operator. This normalized graph Laplacian relates to the unnormalised graph Laplacian, L, through

$$L' = D^{-1/2}LD^{-1/2} \tag{3}$$

and

$$L = \frac{1}{2}[(D - A) + (D - A)^T] \tag{4}$$

where D is the diagonal degree matrix and A is the adjacency matrix, i.e., the connectome. As with the geometric eigenmodes, the connectome eigenvalues and eigenmodes were ordered by decreasing wavelength. The 1019 brain region connectome (1000 cortical regions with 19 subcortical regions) was used as the adjacency matrix, with the 19 subcortical regions removed to obtain a 1000 region source space (comparable to the geometric source space).

2.3 | Source Localization

In their original form, the eigenmodes represent neural activity in neural source space. The transformation from source space to EEG measurement space can be described by a linear forward model under the quasi-static assumption [5, 6],

$$y = Fx + \epsilon \tag{5}$$

where the transformation matrix $F \in \mathbb{R}^{M\times N}$ (known as the forward matrix or lead field matrix) maps any neural activity in source space $x \in \mathbb{R}^{N\times T}$ to sensor space $y \in \mathbb{R}^{M\times T}$. The dimensions represent the number of sensors (M), the number of possible sources in the brain (N), and the number of time steps (T), while ϵ is a matrix representing the overall measurement noise for each time step. For the purposes of EEG source localization, the quasi-static condition holds true as it had been shown that charge does

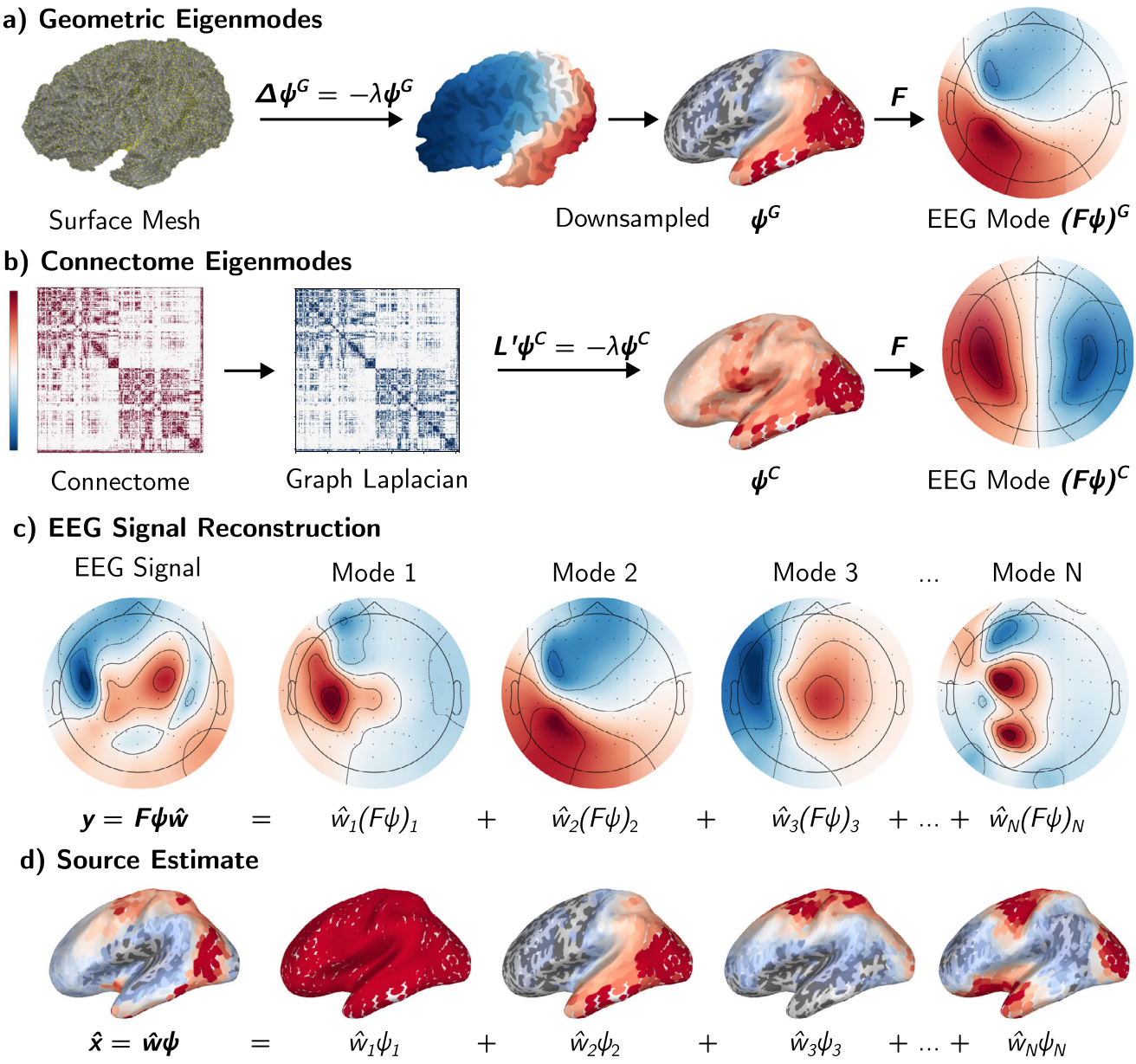

FIGURE 1 | Creation of Structural Eigenmodes and Source Estimation. (a) Following Equation (1), geometric eigenmodes (ψ^G) are generated by solving the eigenvalue problem of the Laplace-Beltrami operator on the surface MRI mesh. This is downsampled to a 1000 discrete cortical region space. The forward operator (F) is applied to transform the eigenmode from source space to EEG space to produce a corresponding set of EEG modes. (b) Following Equation (2), connectome eigenmodes (ψ^C) are directly generated in the 1000 cortical region space by solving the eigenvalue problem on the graph Laplacian representation of the 1019 region connectome and then truncating to cortical regions only. (c) Following Equation (6), the EEG signal can be decomposed into a weighted sum of the different EEG modes. The aim is to find the weights ($\hat{w}$) as given by Equation (7). (d) Finally, the source estimate ($\hat{x}$) can be constructed as a weighted sum of the estimated weights and the corresponding structural eigenmodes in source space.

not accumulate in the extracellular space for the frequency range of signals measured with EEG [6], meaning that for each instance in time, all electric and magnetic fields are dependent only on the active electric source [4].

For this study, F was constructed with a head volume conduction model computed using a three-shell Boundary Element Method (BEM) [48] approach implemented in OpenMEEG and MNE-Python [49, 50]. M, the number of sensors, varies dependent on the EEG-spacing montage used, such that 10-20 spacing involves 21 electrodes, 10-10 spacing involves 88 electrodes, 10-05 spacing involves 339 electrodes. Unless specified, the 10-10 spacing montage was used. N, the number of sources, was set to 1000 dipoles centred at each cortical region in the Yan-Atlas and representing an average spacing close to 1 cm.

Applying the lead field matrix, F, to the set of structural eigenmodes, $\psi \in \mathbb{R}^{N\times K}$, provided a corresponding set of $K \times$ EEG modes. Hence, Equation (5) becomes

$$y = F\psi w + \epsilon, \tag{6}$$

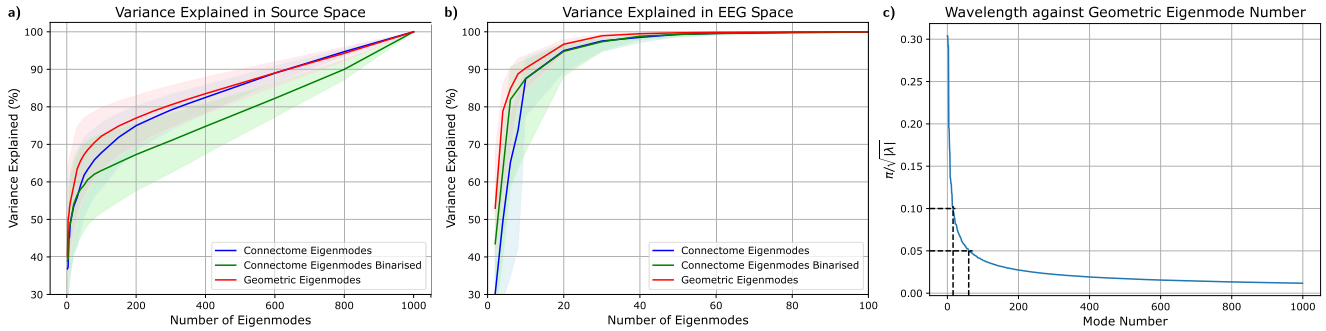

FIGURE 3 | Reconstruction of activity at source and sensor level. For subfigures (a) and (b), variance explained is graphed against an increasing number of eigenmodes used in the reconstruction. No weighting was applied to the eigenmodes. The blue line indicates connectome eigenmodes, green indicates connectome eigenmodes generated with a binarised version of the connectome, and red indicates geometric eigenmodes. The shaded regions indicate the range of variance explained across all ($n = 2038$) simulations. (a) Variance explained in source space shows how well each structural eigenmode type is able to reconstruct the source simulation from the Epileptor model. (b) Variance explained in EEG space indicates how well each structural eigenmode type is able to reconstruct the simulation after it is converted into EEG space using a forward model. The EEG montage used was 10-05 spacing (343 electrodes) for explanatory purposes. Note the difference in x-axis limits due to how quickly the variance explained reaches 100% in EEG space. (c) The wavelength of the geometric eigenmode represented as a proportion of the head dimension. The 0^{th} eigenvalue is ignored. The dashed lines correspond to common EEG montages of 10% and 5% spacing. The corresponding mode numbers are 16 and 60.

where $F\psi$ represents the matrix of EEG modes ($M \times K$) and $w \in \mathbb{R}^K$ is the corresponding weight vector. The least squares solution to Equation (6) is

$$\hat{w} = (F\psi)^{+} y = VSU^T y \tag{7}$$

where the + operator denotes the Moore-Penrose pseudoinverse, obtained via the singular value decomposition (SVD) into rotational matrices U, V^T and a diagonal non-negative real matrix S. It is known that lower spatial modes dominate cortical activity [9], so we biased the eigenmodes ($\tilde{\psi}$) by normalizing by the Froebius norm and then multiplying with a diagonal weighting matrix (W), whose elements are defined by

$$W_i = \frac{1}{|\lambda_i|^{\beta} + c} \tag{8}$$

where c is a constant term to ensure numerical stability and $|\lambda|^{\beta}$ is the mean of the absolute value of the i-th eigenvalue to the power of β. For the geometric eigenmodes, we set $\beta = \frac{1}{2}$ such that the weighting was $\frac{1}{\sqrt{\lambda_i}}$. The rationale lies from the spherical harmonic equations, where $\frac{\pi}{\sqrt{\lambda_i}}$ represents the normalized spatial wavelength of the i-th eigenmode expressed as a fraction of the head diameter. Hence, this weighting aligns with the low-pass filtering properties of EEG through the physical meaning of the normalized spatial wavelength and can be seen as a proxy for the fraction of EEG sensors that can meaningfully capture each eigenmode (see Figure 3). The constant c can then be set naturally as 2π, since the geometric eigenmodes were defined on a hemisphere, resulting in the weight of the 0^{th} (constant) eigenmodes being $1/2$, representing half of the head. For the connectome eigenmodes, the eigenvalues did not had an explicit spatial interpretation in metric units, so we set $\beta = 1$ and $c = 0.1\overline{|\lambda_i|}$, where $\overline{|\lambda|}$ is the mean of the absolute value of all eigenvalues, resulting in weights that closely align with the geometric eigenmode weights after normalization (see Figure S3).

Finally, $\tilde{\psi}\hat{w}$ represents the weighted sums of the biased structural eigenmodes, so everything was combined to yield the aggregate estimated source activity,

$$\hat{x} = \tilde{\psi}\hat{w} = \psi WVSU^T y \tag{9}$$

It was important to consider the singular values of the EEG modes due to the effects of noise and modal amplification [51]. Small singular values apply a large weight to their respective component, leading to any perturbations being significantly amplified. Under the SVD framework, small singular values in S are used to determine modes to truncate in U, V, referred to as the 'rcond' parameter in numpy.linalg. Truncation performs a similar role to the regularization parameter (α or λ^2) in traditional regularization approaches to deal with noise. Unless stated, we set the threshold to $10^{-SNR/10}$, based on the typical regularization value used in minimum-norm approaches.

2.4 | Simulated Evaluation Data

Simulations of seizure activity, generated from connected neural mass models, were used to represent neural activity at the source level. Using the previously mentioned forward model (see Equation (5)), the "ground truth" neural source activity was converted into EEG sensor space. As a result, a simulated dataset, consisting of both macroscale electrophysiological data as well as a corresponding ground truth, could be used to evaluate our source localization approach.

The interconnected neural mass models were defined according to the Epileptor equations [52, 53], an established model that had been widely used to describe the source and spread of epileptic activity with direct usage in clinical trials (EPINOV) [54, 55]. The purpose of using the Epileptor model in conjunction with the connectome was to ensure simulations that were representative of plausible neural dynamics, in which activity propagates across anatomical pathways rather than being spatially unstructured. This design ensured that the simulated data contain spatiotempo-

ral features consistent with known structure–function coupling in epilepsy [35, 56] and the brain in general [34, 57]. This design directly tests the hypothesis that structural eigenmode–based source imaging could exploit such spatiotemporal features to reconstruct underlying neural sources. The simulation pipeline is described below.

2.4.1 | Epileptor Equations

The most common implementation of the Epileptor model, as implemented in the Virtual Brain Project (TVB) [57], characterizes the dynamical behavior of epileptic seizures using five state variables (x_1, y_1, x_2, y_2, z) plus a dummy variable (u) within region i [53]. The equations are:

$$\begin{aligned}
\dot{x}_1 &= y_1 - f_1(x_1, x_2, z) - z + I_{rest,1} \\
\dot{y}_1 &= y_0 - 5x_1^2 - y_1 \\
\tau_0 \dot{z} &= 4(x_1 - x_0) - z + J \\
\dot{x}_2 &= -y_2 + x_2 - x_2^3 + I_{rest,2} + 2u - 0.3(z - 3.5) \\
\tau_2 \dot{y}_2 &= -y_2 + f_2(x_2) \\
\dot{u} &= -\gamma(u - 0.1x_1)
\end{aligned} \tag{10}$$

where:

$$f_1(x_1, x_2, z) = \begin{cases} x_1^3 - 3x_1^2 & \text{if } x_1 < 0 \\ (x_2 - 0.6(z-4)^2)x_1 & \text{otherwise} \end{cases}$$

$$f_2(x_2) = \begin{cases} 0 & \text{if } x_2 < -0.25 \\ 6(x_2 + 0.25) & \text{otherwise} \end{cases}$$

$$J = -g \sum_{j=1}^{N} W_{ij}[x_{1,j}(t - \tau_{ij}) - x_{1,i}(t)]$$

and $x_1(t), y_1(t)$ govern the rapid discharges on the fast timescale, $x_2(t), y_2(t)$ govern spike-and-waves on the intermediate timescale, $z(t)$ is the permittivity variable that operates on a slow timescale affecting the transition between seizure and non-seizure states, $u(t)$ is a dummy variable for low-pass filtering signals from x_1 to x_2, x_0, y_0 are threshold constants, $I_{rest,1}$ and $I_{rest,2}$ are constant injection currents, γ is the time constant of the low-pass filter, τ_0 and τ_2 are time constants, τ_{ij} is the time delay into region i from j based on the streamline lengths, J is the current coupling into region i from other regions j, g is a global coupling strength parameter, and W_{ij} are the coupling weights as defined in the structural connectivity matrix into region i from region j.

These equations were used to generate time series that represent neural activity at each brain region. To represent extracellular dipole sources (x), the above equations are modified to become

$$x = (x_1 - x_2 - b) \times 10^{-8} \tag{11}$$

where $x_1 - x_2$ is used instead of $x_2 - x_1$, as in [52], to ensure that the seizure state has a positive orientation, and 10^{-8} converts to units of Am. Notably, b is a baseline constant, subtracted from the Epileptor model in its original form, to ensure dipole sources maintain approximately zero baseline activity, as expected from the Debye shielding of ions in the electrolyte solution of the extracellular space [4].

2.4.2 | Seizure Simulation

The simulations used 1019 coupled masses of the Epileptor models, as defined in Equation (10), through the coupling current J. The connectivity weight matrix W_{ij} was defined by the 1019 region connectome streamline counts (see Section 2.1) on a specific subject (HCP100206). The axonal time delays τ_{ij} was defined by the 1019 region connectome streamline lengths divided by a conduction speed of 3 m s^{-1} [58]. A Heun's stochastic integrator was used with Gaussian additive noise ($\sim N(0, \sigma^2)$) added to the variables x_2 and y_2 [35, 52]. An integration step size (Δt) of 0.05 was used. To match the temporal properties of focal seizures, the timescale of the model output was scaled such that 256 time steps correspond to 1 s as similarly done by Ref.[53]. Seizure simulations were chosen to last 1 min to allow sufficient epileptogenic activity to develop (Figure 2).

To generate each simulation, a single given region was first defined as the 'epileptogenic zone'. All regions other than the epileptogenic zone were set to have excitability of $x_0 = -2.1$, i.e., tuned to be at the cusp of a bifurcation [35, 59]. To trigger a seizure, the excitability (x_0) of the specified epileptogenic zone was increased to −1.6. The global coupling strength (g) was set to $g = 1.5$ or $g = 2$ to obtain two different degrees of seizure spread. In total, 2038 simulations were generated to produce a dataset with variations in seizure morphology by changing the specified epileptogenic zone and the global coupling strength.

2.4.3 | Mapping to Sensor Space with MNE Python

The source space was defined on the cortical surface such that the centre of each cortical region of the Yan-1000 parcellation was approximated as a dipole oriented normal to the cortical surface. Fixed dipole orientation is widely adopted in literature [20, 21] for reasons of interpretability and numerical efficiency, and aligns with neuroscientific understanding that the dominant contributors to EEG are pyramidal neurons, whose net dipole moments are predominantly oriented normal to the cortical surface [4]. Seizure (Epileptor neural mass model) simulations were mapped directly to source space based on the cortical parcellation of the subject (either HCP100206 or fsaverage). These source space simulations were then mapped into EEG sensor space using OpenMEEG's [49] implementation of the Boundary Element Method (BEM) for the forward problem with the corresponding forward model for the subject. The BEM model consisted of three concentric layers, with standard conductivity values assigned as 0.3 Sm^{-1} (skin), 0.006 Sm^{-1} (skull), and 0.3 Sm^{-1} (cortex) [50]. For solving the inverse problem, the group-average forward model may be used to replicate a real-world scenario where the forward model is not known. The number of sensors varies depending on the EEG-spacing montage used, such that 10-20 spacing involves 21 electrodes, 10-10 spacing involves 88 electrodes, 10-05 spacing involves 339 electrodes.

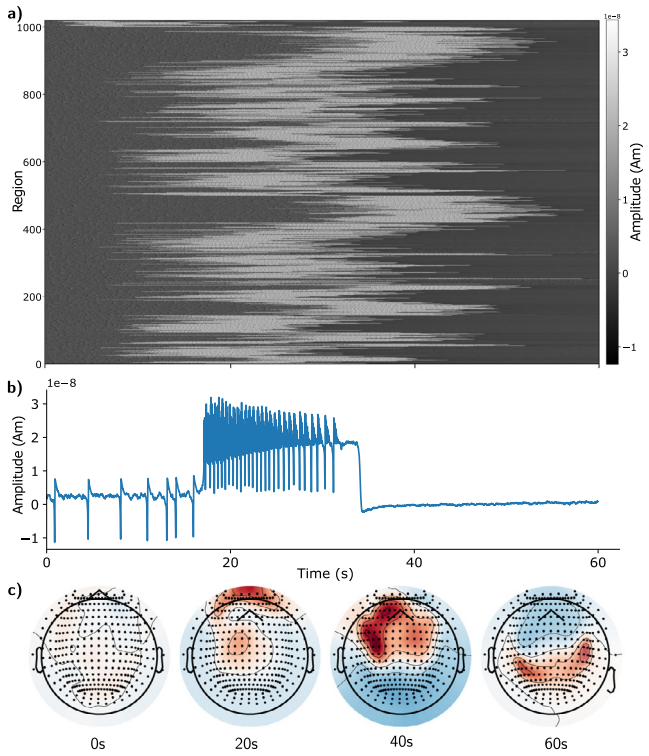

FIGURE 2 | Example Seizure Simulation of the Epileptor Model. (a) Carpet plot [34] of a seizure simulation starting from the thalamus with connectivity strength, $g = 2$. The areas in white signify that the region is undergoing high-energy, epileptic activity. At $g = 2$, the seizure spreads throughout the entire brain. (b) Example time series of the Epileptor model. Key features are the interictal spikes (which go to ~ -10 nAm), the spike-wave discharges at ~ 20 nAm, and the lack of any interictal spikes in the refractory period afterwards. Please refer to the original paper for a comprehensive comparison of the simulated time series with invasive recordings in zebrafish and human [52]. Note that, as per Equation (11), the original equations were adjusted such that the time series have baseline at around 0 and the seizure state is positive. (c) Example of EEG topography. Using the forward model (Equation (5)), the source-level simulations from panel (a) were projected to the sensor space to generate EEG topographies. The corresponding EEG trace is shown in Figure S2. A neurologist reviewer confirmed that the simulated EEG exhibited clinically consistent features, including focal onset, spatial spread, and temporal evolution with characteristic slowing.

2.5 | Evaluation

2.5.1 | Simulation Metrics

Four evaluation metrics were used to assess the accuracy of source localization within the simulations. These metrics are as follows:

2.5.1.1 | Cosine Score.

$$COS = \frac{\hat{x} \cdot x}{||\hat{x}||||x||} \tag{12}$$

where x is the true signal and $\hat{x}$ is the source estimate. Depending on the figure, this may be presented for each time point or averaged across time. Cosine score captures relative distributional accuracy, reflecting how well the relative pattern of activation across the source space matches the true activity.

2.5.1.2 | Normalized Residual Sum of Squares.

$$nRSS = \sum_i \left(\frac{\hat{x}}{\max(|\hat{x}|)} - \frac{x}{\max(|x|)} \right)^2 \tag{13}$$

where the data was normalized with the max to compare across methods with differing units.

2.5.1.3 | Variance Explained.

$$VAR = 1 - \frac{\Sigma_i(\hat{x} - x)^2}{\Sigma_i x^2} = 1 - \frac{nRSS}{SS} \tag{14}$$

where $nRSS$ are the residual sum of squares and SS are the sum of squares over all possible sources i in source space, and the max normalization is performed as above. We note that, for our specific signal, a baseline constant was already identified and subtracted (see Equation (11)) such that the baseline for x was at 0.

2.5.1.4 | Region Localization Error.

$$RLE = \frac{1}{2Q} \sum_{k \in I} \min_{l \in \hat{I}} ||r_k - r_l|| + \frac{1}{2\hat{Q}} \sum_{l \in \hat{I}} \min_{k \in I} ||r_k - r_l|| \tag{15}$$

where I and $\hat{I}$ represent the true and estimated indexes of active sources, respectively, Q and $\hat{Q}$ represent the number of true and estimated active sources, and r_k denotes the position of the k-th dipole source in space as per MNE-Python's implementation [50]. Sufficiently active sources are algorithmically identified to be beyond Otsu's Threshold [60], as suggested by [22, 61]. The region localization error was computed across time as well as at 50% of maximum EEG power, representing a sensible extent of seizure spread and the rising phase of a seizure [23]. Region localization error captures spatial accuracy, reflecting how precisely the estimated source activity was positioned in space.

2.5.2 | Simulation Test Conditions

To ensure experimental rigour, we performed four complementary evaluations, designed to test the comparative performance, biological plausibility, and robustness of the structural eigenmodes approach. Statistical significance was assessed with a paired Wilcoxon signed-rank test between the geometric eigenmode approach and alternative approaches. These test conditions are as follows.

1. Benchmarking with other algorithms
   To benchmark, we compared different off-the-shelf source localization algorithms (dSPM, MNE, sLORETA, and eLORETA) on our dataset as implemented in MNE-Python [50].
2. Surrogate mode testing
   We applied a surrogate mode test to assess whether the original eigenmodes performed significantly better than structurally similar alternatives. Surrogate modes were generated using two approaches: roll, which applies a cyclic shift

to all eigenmodes using NumPy's roll function (preserving orthogonality), and rotation, which applied orthogonal rotation matrices within each harmonic group, preserving their internal spatial structure, following the method of Ref.[62]. For each simulation, we computed a performance score for the original eigenmodes and compared it to the distribution of surrogate scores. The percentile rank of the original mode relative to the surrogate distribution was calculated for each simulation. To assess whether the original modes consistently outperformed surrogates across simulations, we applied a paired Wilcoxon signed-rank test on the percentile values (centered around chance level by subtracting 50).

3. Subject-specific versus group-average comparison
The inverse crime method [63] is referred to as such when the same model was used for both the forward and inverse solutions. To test the extent of this, we tested simulations where the signal in Equation (5) was generated with the subject-specific forward model and the inverse used a group-average forward model (fsaverage); i.e., the EEG modes in Equation (6) were created using the group-average forward. We also tested the effect of using fsaverage to generate the geometric eigenmodes and a HCP group-averaged connectome to generate the connectome eigenmodes.

4. Varying signal-to-noise conditions for EEG
EEG is well-known to be a noisy signal in practice. To simulate the challenge of noise contamination, Gaussian white noise was added to the EEG signal with a signal-to-noise ratio of 3 dB, 10 dB, or None (signifying no white noise added). The standard deviation of the noise was given by $\sigma_{Noise} = P_{Signal}/\sqrt{10^{\frac{SNR}{10}}}$.

For a more direct comparison with previous literature, which focuses typically on one to few sources of various extent [21, 24–28], the interested reader can refer to the evaluation on a simple set of single-patch simulations in Section S1.1. These patch simulations were also more analogous to the interictal spikes analyzed in the following section with real patient data. In addition, to assess whether the results obtained in the lower resolution source space held at a higher spatial resolution, further testing was conducted using a source space consisting of 10 242 dipoles per hemisphere (icosahedron 5 spacing), with eigenmodes computed at this resolution (see Section S1.3).

2.5.3 | Real Data

With simulation, we tested the eigenmode approach to source localization under different conditions and identified how best to use the approach. Next, the eigenmode approach was validated in a cohort of 20 drug-resistant, focal epilepsy patients who had undergone resective surgery to obtain seizure-freedom as per ILAE-1 or ILAE-2 classification. The data [22] had high-density 76-channel scalp EEG recordings where 5 to 90 interictal spikes were identified and averaged per patient. All data processing was performed by the data creators. Averaged interictal spikes per patient were input into the eigenmode algorithm with a group-average model and then compared to the clinical records of resected area. A signal-to-noise ratio of $10log_{10}(N)$, where N was the number of interictal spikes, was assumed for each patient. The resected region was mapped onto the group-averaged source space (fsaverage) and treated as the base truth. This 'ground truth' was compared to the estimate produced by the geometric/connectome eigenmode source localization approaches using geometric/connectome eigenmodes generated from group-averaged data.

Given that the task was a binary classification, for better comparison with the original paper, we evaluated the following metrics in this section: region localization error (RLE), precision, recall, and the area under the receiver operating characteristic curve (ROC-AUC). Let TP denote true positives, FP false positives, FN false negatives, and TN true negatives. Then, precision and recall are defined as

$$\text{Precision} = \frac{TP}{TP + FP}, \qquad \text{Recall} = \frac{TP}{TP + FN} \tag{16}$$

As with simulation, Otsu's threshold was used to determine the appropriate threshold to use for these threshold-based metrics.

In contrast, the ROC-AUC evaluates the ability of the classifier to discriminate between positive and negative classes across all possible thresholds. The ROC curve plots the true positive rate ($TPR = \frac{TP}{TP+FN}$) against the false positive rate ($FPR = \frac{FP}{FP+TN}$), and the AUC quantifies the area under this curve. A perfect algorithm achieves an AUC of 1, while a random algorithm has an expected AUC of 0.5.

2.5.4 | Ethics Statement

Ethical approval was not required for this study. The primary analyzes were conducted using simulated data. In addition, the analyzes involving human data used publicly available, de-identified datasets, which were exempt from ethical review under Section 5.1.17a of the NHMRC National Statement on Ethical Conduct in Human Research.

2.5.5 | Statistical Analysis

The source localization results were described as mean and standard deviation. All data preprocessing in the real, epileptic patient dataset was performed by the original data creators. For the real dataset, the sample size was $n = 20$ patients. For the simulated dataset, the sample size was $n = 2038$ simulations. The one-sided paired Wilcoxon signed rank test was used for the statistical tests and performed in Python 3.10.

3 | Results

3.1 | Structural Eigenmodes Represent Simulated Cortical Source Activity

First, it is vital to confirm that simulations of ictal activity can be decomposed into structural eigenmodes. This is demonstrated by Figure 3, which shows that a relatively small number of eigenmodes were required to reconstruct the simulations in both EEG and source space.

In terms of source-space reconstruction (Figure 3a), both geometric and connectome eigenmodes were able to represent a significant portion (75% and 77%, respectively) of the simulated source signal using 200 eigenmodes. The results were consistent with previous work using structural eigenmodes to reconstruct fMRI data, which is more analogous to source-space than EEG signals, with >80% reconstruction accuracy using 200 eigenmodes for a single hemisphere [9]. It is interesting to note that, whilst it is common to binarise the connectome before using it [34, 64], we find that the binarised connectome had poorer explanatory power in source-space than the non-binarized connectome eigenmodes, agreeing with recent articles that binarization may be too simplistic and removes valuable information [65]. At low numbers of eigenmodes, geometric eigenmodes appeared to have higher explanatory power than connectome eigenmodes (at 50 eigenmodes, 62% vs. 77%). This gap then disappeared as more eigenmodes were introduced.

In terms of EEG-space reconstruction (Figure 3b), under no-noise conditions, both connectome eigenmodes and geometric eigenmodes were able to reconstruct beyond 90% of the variance of an EEG signal with only 20 eigenmodes across both hemispheres. Performance quickly reached 100% variance explained, reflecting the high correlation between EEG electrodes and the presence of low singular values in the SVD of the EEG-mode space. This trend, where the variance explained quickly saturates, aligns with the physical interpretation of the eigenvalues of the geometric eigenmodes as spatial frequencies, as demonstrated by Figure 3c). More specifically, the spatial wavelength is constructed through the relation $\frac{\pi}{\sqrt{\lambda}}$, which can be interpreted as modes that span the same spacing as the EEG electrodes. A spacing of 5%, as per a 10-05 montage, would be expected to saturate in complexity at around 60 modes, as demonstrated by Figure 3b,c.

3.2 | Structural Eigenmodes Enable Source Localization of Seizure Spread

Next, we compared the accuracy when geometric and connectome eigenmodes were used to predict the underlying neural sources. The following sections present a detailed evaluation of the performance of the structural eigenmode approach when using a different number of modes, under different signal to noise ratios, and when compared to other approaches. Figure 4 provides a visual representation of an example simulation, where both structural eigenmode approaches were able to track the spread of a seizure originating from the thalamus.

3.2.1 | Performance Against Number of Modes — The Over- Versus Under-Parameterized Regimes

Figure 5 depicts the effects on localization performance as the number of modes increases. With no simulated EEG noise and no truncation, increasing the number of modes initially improves most metrics (RLE at 50% power and cosine score), before reaching a peak and deteriorating. For the cosine score and for geometric eigenmodes, this local peak is at 32 modes, corresponding to four eigengroups per hemisphere. All metrics show progressively worse performance, until a local maxima/minima, corresponding to 88, the number of electrodes under the standard 10-10 EEG layout. After reaching 88 electrodes, performance then begins to improve until it reaches a plateau. This trend is heavily related to the 'Double Descent' phenomena seen in machine learning (as discussed in Section 4.5) [66, 67].

Comparing geometric and connectome eigenmodes, both types of structural eigenmodes appear to perform similarly well under all noise conditions but with some notable differences. For RLE at 50% of EEG power, connectome eigenmodes appear to be slightly better under no noise conditions by 1 mm. For averaged cosine score, geometric eigenmodes reach the optimal under a lower number of modes, mirroring expectations from Figure 3a. For cosine across time, before the 10 s mark when the seizure has not spread to too many regions, geometric eigenmodes had a higher score under high noise conditions. This is likely due to the geometric eigenmodes using a fewer number of low-wavelength modes to explain the data and thus being slightly less affected by noise.

These results were consistent when using EEG 10-05 spacing consisting of 339 electrodes and EEG 10-20 spacing consisting of 21 electrodes, and when both the geometric and connectome eigenmodes were used in conjunction (see Sections S1.2 and S1.6). Overall, the results of this section suggest that there are two sensible choices for the number of modes, whether it be the under-parameterized or over-parameterized regime, provided the choice is far from the number of electrodes of the EEG montage. The remainder of the presented results used 1000 eigenmodes (unless otherwise stated) to take advantage of over-parameterization.

3.2.2 | Testing, Validation, and Comparison to Other Approaches

The performance of different variations of the source location approaches is shown in Figure 6, with the mean and standard deviation provided in Table S1. Under high noise conditions ($SNR = 3$ dB), all methods performed relatively poorly, with the cosine score having a large deviation and below 0.40. Therefore, the evaluation was conducted under optimal and medium ($SNR = 10$ dB) noise conditions. Statistically significant differences in performance metrics between the geometric eigenmode approach and alternative methods were evaluated using signed-rank test with a p-value < 0.01.

3.2.2.1 | Performance of Established Methods. For all signal-to-noise ratios, the established methods (dSPM, MNE, sLORETA, eLORETA) were unable to track the progression of a seizure in the simulated dataset. This is evidenced by the relatively poor cosine score and variance explained at around 0 or lower. The primary issue is that the methods were unable to determine the correct polarity of one-sided simulations, wherein seizure states were modelled as positive deflections from the baseline. Section S1.7 demonstrates that by applying a loose orientation or by taking the absolute value of the estimates, the metrics increase substantially, but this can be considered a misleading improvement given that the polarity of the estimate is known to be incorrect. Section S1.6 displays that using 10-

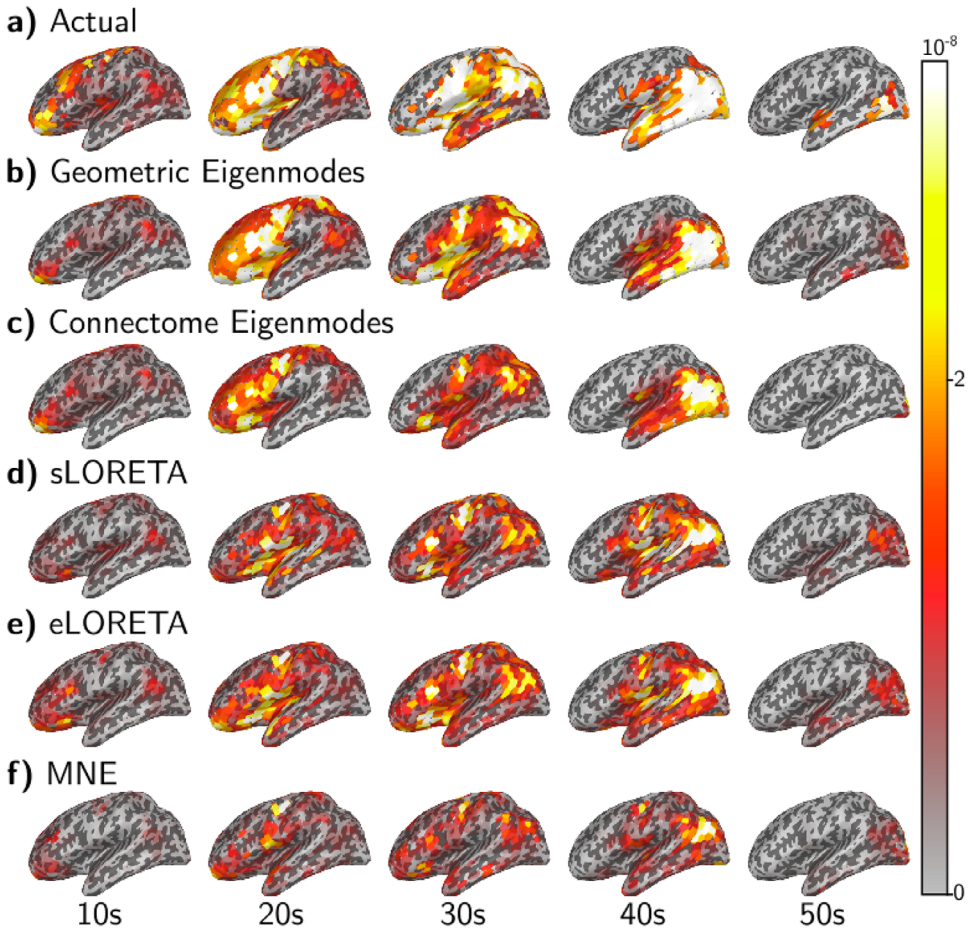

FIGURE 4 | Source localization example for seizure originating from thalamus plotted on left hemisphere. Five time points are selected in increments of 10 s and visualized on the left hemisphere. For the right hemisphere result, please see Figure S16. 50% EEG power for this simulation occurs at the 30 s. The colour scale is set such that maximum amplitude is white, progressing to yellow, orange, red, and transparent for 0. (a) The actual or 'ground truth' source activity generated from the Epileptor model. As time progresses, the seizure spreads from the anterior to posterior regions of the brain. During this time, different areas of the brain are activated in varying spatial extents and patterns. (b) & (c) Both geometric eigenmodes and connectome eigenmodes are able to perform reasonably well in sparse activations (10 and 50 s), as well as dispersed activations (20 to 40 s). (d–f) The LORETA family predict more focal sources with regularization parameter set according to the $10^{-SNR/10}$ heuristic. For visualization and to improve performance, the orientation of the dipole was allowed to be loose for the LORETA family, which we demonstrate to be near equivalent to taking the absolute value of a fixed orientation estimate. As such, the performance increase for the LORETA family can be considered misleading.

05 EEG spacing (343 electrodes), the established methods had a significant increase in performance and were able to determine the correct polarity of the underlying sources.

3.2.2.2 | Comparison Between Structural Eigenmode Approaches. Under optimal no-noise conditions, geometric eigenmodes offered statistically significant performance improvement over connectome eigenmodes. Time-averaged region localization error was 0.12 ± 0.14 mm versus 0.24 ± 0.20 mm, region localization at 50% EEG power was 4.05 ± 2.08 mm versus 4.20 ± 1.85 mm, cosine score was 0.76 ± 0.07 versus 0.74 ± 0.05, mean squared error was 0.028 ± 0.002 versus 0.034 ± 0.007, and variance explained was 0.58 ± 0.10 versus 0.50 ± 0.04 for geometric eigenmodes versus connectome eigenmodes, respectively. Due to using algorithmic thresholding, region localization error can be slightly misleading between methods if a substantially different threshold is chosen as the level of threshold is generally correlated with increasing region localization error. The approximate spacing between regions in the source space was around 10 mm, so an average region localization error below 1 mm is insubstantial. Similar performance trends were observed across varying SNR levels and in the higher resolution source space of 20 484 vertices (see Figure S5), where geometric eigenmodes again exhibited a small advantage in cosine similarity and slightly better performance in explained variance and mean squared error. With decreasing SNR, Figure 6 suggests that the performance of the geometric eigenmodes decreases more than connectome eigenmodes. This is demonstrated to be due to the use of a heuristic for setting the truncation parameter. For analysis on this situation and the results under optimised conditions, we refer to reader to look at Section S1.4 and Figure S8.

3.2.2.3 | Effect of using Subject-Specific Versus Group-Averaged Structural Data. For geometric eigenmodes, using subject-specific eigenmodes did not offer statistically significant improvement in RLE, RLE at 50% power or cosine score. For mean squared error and variance explained, there was a small improvement of $< 1\%$ that was statistically significant.

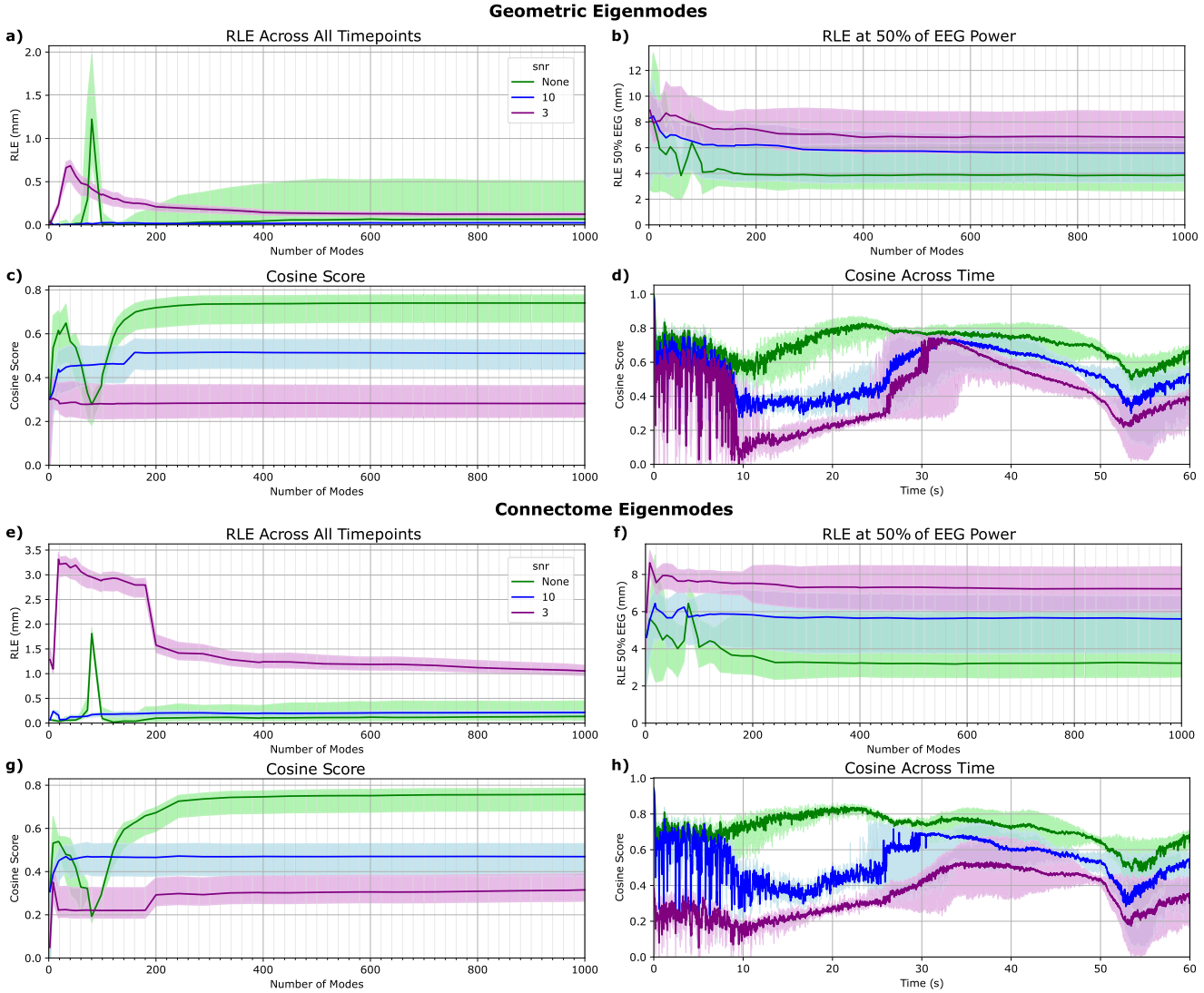

FIGURE 5 | Geometric and connectome eigenmode metrics against number of modes and signal to noise conditions Four different metrics: (a) & (e) region localization error averaged across all timepoints, (b) & (f) region localization error at 50% of EEG power, (c) & (g) cosine score, (d) & (h) cosine score averaged across all timepoints, are shown for both the geometric and connectome eigenmode approaches. The different colored lines represent different levels of EEG noise added to the simulation. A SNR of 'None' signifies no noise was added (green), '10' means a SNR of 10 dB (blue), and '3' means a SNR of 3 dB (purple). Under increasingly noisy conditions, modes are truncated under the SVD framework, hence eliminating double descent. The shaded region about the line signifies the interquartile range for that metric across all simulations ($n = 2038$). The solid line represents the median value of the metric across all simulations for the specific number of modes. For cosine across time, the maximum across all number of modes is taken first before the median and interquartile range is calculated for the figure. The plots shown are for 10-10 EEG spacing, consisting of 88 electrodes.

Using the group forward model resulted in a performance decrease of around 30% under perfect noise conditions but, surprisingly, a 4% increase at a SNR of 10 dB. It is possible that the smoothing of the brain, associated with group-averaged structural data, may have improved noise handling. For the connectome eigenmodes, using subject-specific eigenmodes reduced performance slightly (a cosine score of 0.74 ± 0.05 vs. 0.75 ± 0.05), while using the group forward model dropped the cosine score by 40% to 0.44 ± 0.03. Geometric eigenmodes appeared more robust to perturbations in subjects from the group-average.

3.2.2.4 | Surrogate Modes Test. Both geometric and connectome eigenmodes offered statistically significant improvements over their surrogates for all metrics and for high SNR situations. For geometric eigenmodes, the cosine score was 0.76 ± 0.07 compared to 0.28 ± 0.07 for rolled surrogates and 0.75 ± 0.07 for rotated surrogates. For connectome eigenmodes, the cosine score was 0.74 ± 0.05 compared to 0.26 ± 0.08 for rolled surrogates and 0.62 ± 0.04 for rotated surrogates. The reason why geometric eigenmodes had a much smaller difference in performance compared to its rotational surrogates is due to the methodology of the rotational surrogates. Since the eigenmodes are rotated within their eigengroups (only applicable to geometric eigenmodes), the rotational surrogate method is significantly harsher for the geometric eigenmodes than the connectome eigenmodes, where it is equivalent to a form of spin test.

Additionally, applying the same surrogate test to the geometric eigenmodes constructed in a higher-dimensional source space (ico-5 spacing with 20 484 sources) revealed a more substantial

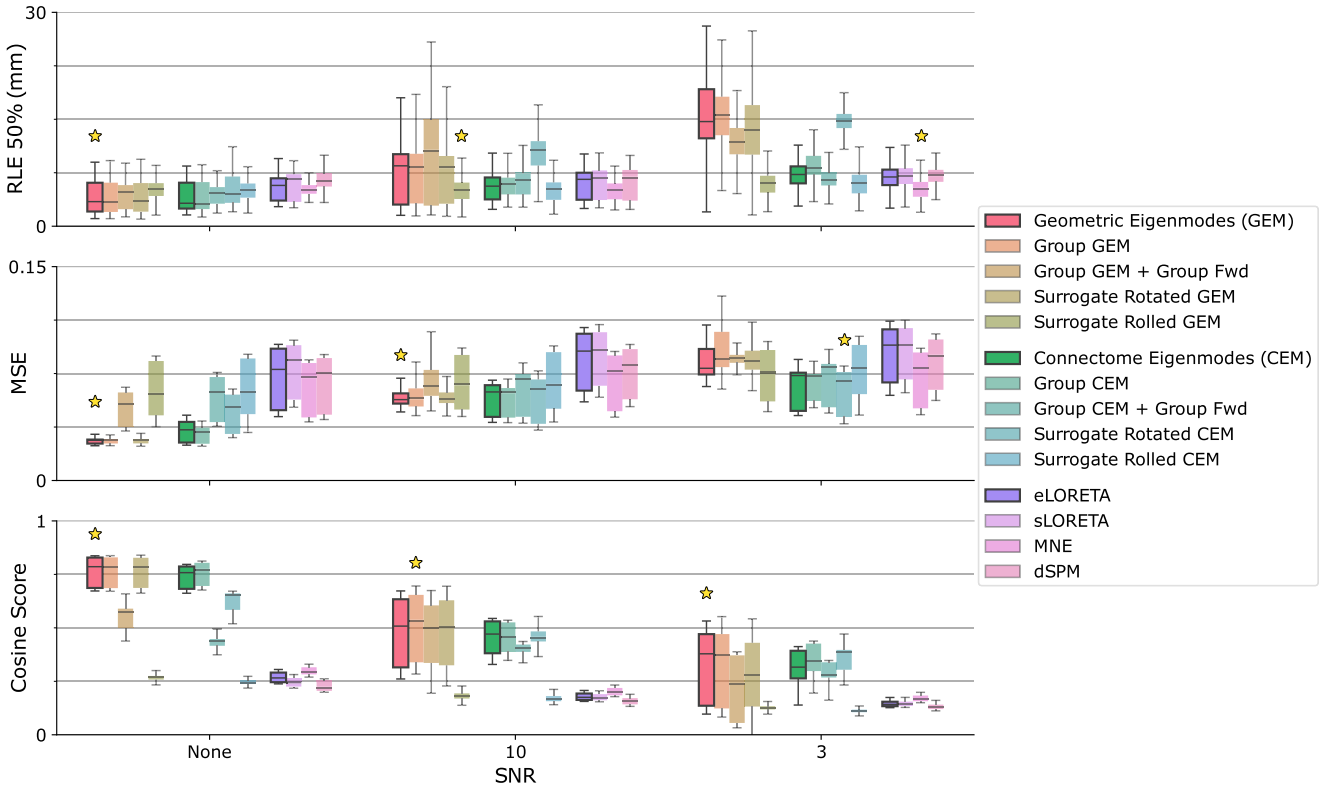

FIGURE 6 | Comparisons of the structural eigenmode approach against all other methods and surrogate testing. Source localization algorithms are grouped based on their type: GEM (geometric eigenmodes), CEM (connectome eigenmodes), and comparison methods. These algorithms were evaluated across all $n = 2038$ seizure simulations. The highlighted boxplots correspond to the base method for geometric eigenmodes, connectome eigenmodes, and eLoreta for a standard comparison under normal conditions. The box shows the quartiles of the dataset, while the whiskers extend to show the rest of the distribution, except for algorithmically determined outliers. Three metrics are graphed: (i) region localization error at 50% EEG power, ii) normalized mean squared error, and (iii) cosine score. The star above the boxplot signifies the algorithm with the best performance for that metric and SNR. For geometric and connectome eigenmodes, eigenmodes generated using group-averaged structural data were tested. The scenario when the subject's MRI scan was not available (where the group-averaged eigenmodes and group-averaged forward model were used together) was also tested. Surrogate eigenmodes were generated for the geometric and connectome eigenmodes as explained in Section 2.

difference in performance between the geometric eigenmodes and its rotational surrogates (see Figure S5). This suggests that the reduction in source space removed much of the finer-resolution spatial information that the geometric eigenmodes provided. Overall, the surrogate eigenmode tests suggest that there is physical meaning in the structural eigenmodes used and that both types were helpful in constraining the problem of source localization.

3.3 | Structural Eigenmodes on Localizing the Epileptogenic Zone in Real Patients

As per [22], we localized the averaged interictal spike data of 20 patients who suffered from drug-resistant focal epilepsy and underwent resective surgery, where the resected region is treated as the base truth and compared to the estimate produced by the source localization approaches. This is an imperfect source of truth, as areas that were active during interictal activity may lie outside of the resected region, and the resected region will be likely larger than the active area. Nevertheless, it is still suitable as a means to compare different source localization approaches, as the resected region is highly likely to be the majority of the source of the interictal activity.

The geometric eigenmode approach had significantly higher recall compared to other methods (Figure 7), at no expense to other metrics, region localization error, precision, and ROCAUC (Receiver Operating Characteristic Area Under the Curve). Using the paired one-sided Wilcoxon signed rank test, comparisons had p-values of 0.0133 against connectome eigenmodes, 0.0068 against sLORETA and 0.0088 against eLORETA. This 30% improvement in recall against traditional approaches suggests that geometric eigenmodes have superior spatial coverage of the true source without overextending beyond the predominant region of interictal activity. An improvement in recall without penalty to other aspects in performance is an advancement compared to previous approaches, which needed to balance a trade-off between precision and recall between algorithms [22, 26, 68]. The relative performance increase of geometric eigenmodes against connectome eigenmodes mirror simulation results to suggest that group-level geometric eigenmodes should be preferred over using group-averaged connectomes.

4 | Discussion

The presented results demonstrated that structural eigenmodes offer a computationally efficient means to estimate biologi-

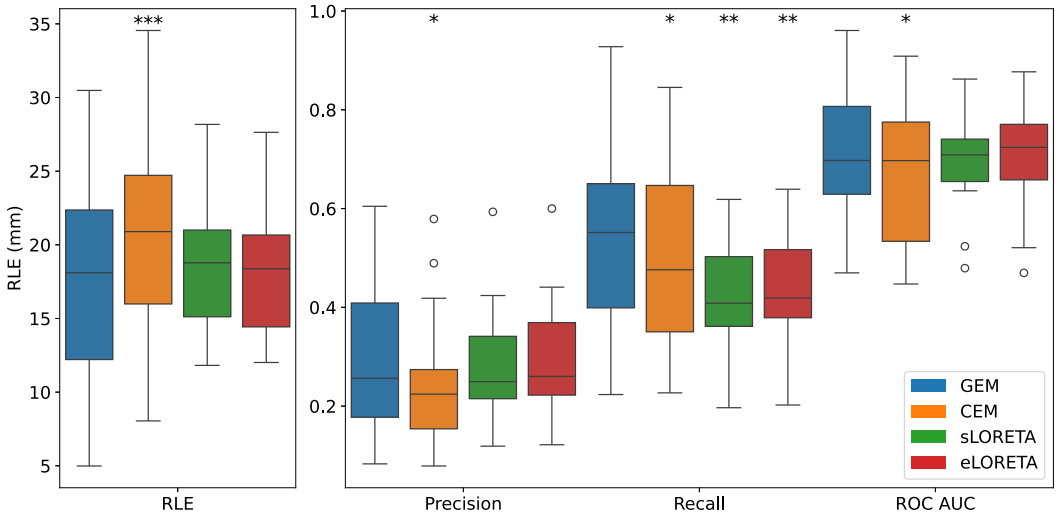

FIGURE 7 | EEG 10-10 spacing clinical validation in 20 drug-resistant epilepsy patients in comparison with surgical resection. The boxplots demonstrate the range of values for the different metrics and source localization algorithms for a group of $n = 20$ patients. The whiskers extend to the minimum and maximum values, except for algorithmically determined outliers, which are denoted as circles. The box contains the interquartile range, with the horizontal line inside the box denoting the mean. For GEM region, localization error was 17.41 ± 7.77 mm, precision was 0.29 ± 0.16, recall was 0.56 ± 0.17, and ROC AUC was 0.72 ± 0.15. For CEM region, localization error was 20.76 ± 6.52 mm, precision was 0.25 ± 0.14, recall was 0.50 ± 0.19, and ROC AUC was 0.67 ± 0.15. The asterisks (*) above the boxplots indicate the level of statistical significance between the geometric eigenmode approach and the corresponding method using the one-sided Wilcoxon signed rank test, with $^*p < 0.05$, $^{**}p < 0.01$, $^{***}p < 0.001$. Recall for GEM was found to be significantly higher than sLoreta and eLoreta at an $\alpha = 0.01$. The other metrics had no statistically significant differences and were comparable.

cally feasible sources, with potential application to localizing epileptic activity. Structural eigenmodes were able to represent simulated ictal activity at both source and sensor levels. Surprisingly, few modes were required to explain most of the variance in both source and sensor space, reflecting the fact that low wavelength modes dominate cortical activity [9, 69]. Both geometric and connectome eigenmodes demonstrated potential as efficient constraints for electrophysiological source localization, completing reconstructions within a fraction of the signal time. Importantly, both approaches provided similarly strong performance and were able to track the spread of a seizure, compared to mainstream approaches, which were unable to do so. This is especially noteworthy for geometric eigenmodes given that the underlying simulations used the same subject-specific connectome as the connectome used to generate the connectome eigenmodes. Contrary to expectations that only a few modes would be required, the current study showed more modes significantly improved performance, most likely related to the 'double descent' phenomenon in machine learning literature [66, 67]. Finally, the geometric eigenmode approach was found to localise the epileptogenic zone successfully in epilepsy patients who had positive surgical outcomes, demonstrating significant alignment between the localization results and the clinical findings.

4.1 | On the Neurological Meaning of Eigenmodes

Previous work on fMRI has suggested that, relative to the entire brain space, both geometric eigenmodes and connectome eigenmodes offer a lower-dimensional and more interpretable view of the mesoscopic scale activity of the brain [9, 13]. This work focused on EEG, which provides a more direct measurement of neural activity and operates on temporal scales that closely align with neural dynamics, in contrast to the slower, indirect BOLD (Blood Oxygen Level Dependent) response measured by fMRI [70]. In simulated and real-world settings, both types of structural eigenmodes were able to find the most relevant spatial modes that reconstructed brain activity. This result held true under surrogate tests, in which the eigenmodes were altered in ways that preserved orthogonality or spatial structure. Hence, this work supports the view that both types of structural eigenmode offer neurologically meaningful interpretations of neural activity beyond acting as simple mathematical constructs.

Subject-specific modes offered performance similar to that of group-averaged modes in this analysis, suggesting that subject-specific modes were not vital to improving performance at the current resolution of 1000 cortical dipoles. This mirrors findings in the original paper, where, in high resolution fMRI data (32 492 vertices per hemisphere), individual-specific eigenmodes offered slight improvements compared to group-template derived eigenmodes in some individuals in reconstructing task-activation maps but not in reconstructing resting-state activity [9]. However, it is non-trivial to align subject and group-averaged spacing correctly. So, from a practical standpoint and to avoid alignment issues, algorithms should be run fully in subject space or group-averaged space. More importantly, weighting the eigenmodes based on wavelength was necessary for good source location performance, supporting previous findings that longer wavelength activity dominates resting-state and task-based activity [9] and enhanced long-range interactions (reflecting functional integration) emerge during interictal epileptic discharges [14]. Future work can consider optimizing the specific weightings, but the weighting schema chosen in this work based on physical principles performed very well.

4.2 | On the Difference Between Geometric Eigenmodes and Connectome Eigenmodes

When used as basis sets to constrain the source localization problem of EEG, both geometric and connectome eigenmodes performed similarly across most metrics, with more noticeable differences emerging in mean squared error and variance explained. This may seem counter-intuitive: why are connectome eigenmodes not consistently superior to geometric eigenmodes despite being evaluated on simulations based on the connectome? A key reason is that although the Epileptor model uses the connectome as a coupling scaffold, the resulting activity is not a simple linear combination of the connectome or its eigenmodes, but is additionally shaped by intrinsic regional dynamics, noise, and nonlinear interactions. Moreover, connectome eigenmodes are derived transformations of the connectome rather than direct representations of the structural coupling itself. Consequently, there is no guarantee that the dominant spatiotemporal patterns of the simulated data align optimally with the connectome eigenmode basis. Indeed, Figure 3a) demonstrated that geometric eigenmodes required less modes to reconstruct seizure activity and exhibit slightly greater explanatory power than their connectome counterparts. The performance of geometric eigenmodes can be understood from an understanding of their derivation from Neural Field Theory [71]. Geometric eigenmodes inherently model an exponential distance-related (EDR-like) propagation structure, which aligns with known anatomical wiring constraints, reflecting the trade-off between abundant short-range connections and costly long-range connections, to support realistic information flow [9, 15].

Given that the eigenmode weighting process, critical to the optimization, was subtly different between the two approaches, and that the construction of the connectome and its eigenmodes require many procedural decisions, we do not consider the observed performance differences to be sufficient to argue for the superiority of one method over the other. Considering these results, we conclude that both geometric and connectome eigenmodes are substitutes in terms of performance, at least for the purposes of EEG source reconstruction. However, from a practical perspective, geometric eigenmodes only require the subject's MRI scan, which is already required by the forward model, whereas connectome eigenmodes require additional data in the form of diffusion MRI and involve additional processing, which may affect the reconstruction results [42]. Indeed, there are complexities in aligning the source space with the streamline to parcellation mapping for connectomes, whereas aligning the source space in the geometric eigenmode approach is trivial. Furthermore, in the case where the subject-specific structural data is not available, our results suggest that geometric eigenmodes offer superior performance when using group-averaged data. As such, geometric eigenmodes may be preferred for the purposes of source localization from a practical and ease-of-use standpoint.

4.3 | On Biologically-Informed Constraints in Source Localization

Traditional approaches have focused on mathematical arguments of smoothness and focality, and were less motivated by neurophysiology [8]. The issue of insufficient biological realism in source localization problems is gaining attention in the field. Complementary studies have typically tried regularization and other methods of incorporating connectome connectivity [20, 72] and cortical geometry [19] with some success. For completeness, we additionally compare the proposed approach with recent eigenmode-based source inversion methods [19, 20] in Section S1.5, where our methodological and optimization improvements can be examined in more detail. Owing to the optimization procedure performed, each evaluated timepoint takes under 1 ms for any modern system to compute making realtime analysis possible.

The other approach is best represented by the seminal work of [22, 61], who introduced the idea of biologically constraining neural networks with simulated data generated from dynamical neural models with great success. However, with deep learning approaches, a problem arises in validation because the simulated training and test data would be very similar, leading to the risk of over-fitting and low generalization. This work shares the advantage of demonstrating complex source reconstruction using similarly complex models but ensures the source of the biological information is separate from the simulated data, making it more likely that this approach is generalizable to other settings. Deep learning methods continue to be an active area for source localization research despite having the notorious requirement of needing to retrain the model on any kind of experimental change such as the electrode montage used [26–28]. In all, this study supports the view that the problem of source localization is significantly aided by biologically informed constraints, and that both geometric and connectome eigenmodes provide relatively high gains for their mathematical simplicity and computational efficiency.

4.4 | On Alternate Formulation - Regularization

This work took advantage of the singular value decomposition of the Moore-Penrose inverse to arrive at the inverse solution. A regularization approach to incorporate structural eigenmodes [19, 20] is also possible, which would align well with current Minimum-Norm approaches from the LORETA family. In such a scenario, the source space solution would instead be given by

$$\psi w = [(F\psi)^T(F\psi) + (\alpha + \alpha_0)R]^{-1}(F\psi)^T y \tag{17}$$

where α is the noise-dependent regularization parameter, α_0 is a regularization constant to ensure numerical stability for all signal-to-noise ratios, and R is the regularization matrix of choice. Examples of R include I, the identity matrix, for Tikhonov regularization to arrive at a derivative of MNE, and L^TL where the Laplacian is used to arrive at a derivative of LORETA. Applying an R matrix dependent on λ to bias the eigenmodes, similar to the W weighting matrix in Equation (8), would be appropriate for the eigenmode source localization approach, where the power (β) of the eigenvalue can be tuned. The more general form of localization using basis field expansions has been previously discussed [8, 25], with approaches using spherical harmonics [25] and, more recently, spherical head harmonics [21]. For our test cases, we found that the Moore-Penrose inverse was easier to work with, while suitable for a wide range of signal-to-noise ratios.

4.5 | On Over-Parameterization in Optimization

The phenomena of overparmeterisation (also referred to as 'double descent' within the machine learning community) refers to the situation where a model has more parameters than necessary to fit the data, typically significantly more [67, 73]. Traditionally, this was expected to lead to overfitting, wherein the model would be dedicating parameters to fitting to noise instead of the true signal, leading to poor generalisability. However, modern deep learning challenges this view in that highly overparameterised models, namely deep neural networks, typically outperform everything else [66].

Within the context of eigenmode source localization, Figure 5 showed that initially, as the number of parameters (modes) increased, performance increased as the model (algorithm) was able to output increasingly complex signals to express the true signal. Then, performance decreased with increasing number of parameters (modes) until the model (optimization) crossed from the under-parameterised ($M < K$) to over-parameterized ($K < M$) regime (where we had more modes than sensors). From that point onwards, the metrics steadily increased. The poor performance when $M \approx K$ was due to the system forcing a solution that fits the sensor signal exactly, but the EEG modes are increasingly aligned in EEG space, as seen in Figure 3b. When $M > K$, the increased solution space meant that there were infinite solutions and hence the minimum norm constraint was applied to return a unique solution. This is thought to have a regularization effect to improve the reconstruction as the number of modes increased [73].

Future work should attempt to take advantage of the benefits and be mindful of the issues related to 'double descent'. For example, incorporating loose orientations would increase the number of parameters by a multiple of 3, which may also lead to improvements explainable by overparameterization, and the number of eigenmodes used should be far away from the number of independent sensors used.

4.6 | On the Implications of Tracking Seizure Propagation and Localising the Epilpetogenic Zone in Patients

From a clinical perspective, the ability to capture the dynamic evolution of seizure activity provides valuable insights beyond static localization of the seizure onset zone. The spatial trajectory and timing of seizure spread may help disambiguate whether a region is truly epileptogenic and part of the origin or is instead part of the downstream propagation path. This distinction is critical for improving surgical planning because removing non-epileptogenic yet early-recruited regions may lead to unnecessary functional deficits without improved seizure control [74]. Additionally, being able to noninvasively model and reconstruct the spatiotemporal structure of seizures opens the door to more responsive and personalised interventions [53, 55]. For instance, real-time tracking of seizure spread could inform closed-loop stimulation paradigms that aim to disrupt propagation before clinical symptoms emerge [75]. In this context, the superior performance of structural eigenmodes in identifying recruited regions implies a potential role for these models in both pre-surgical evaluation and dynamic seizure tracking. With further improvements in source location and experimental technique, these models may even be able to test competing hypotheses of seizure generation and propagation – whether driven by fixed focal sources [76] or recruitment through travelling wavefronts [56, 77, 78].

In terms of better patient outcomes and quality of life, enhanced spatial resolution and interpretability may aid in distinguishing different seizure types, such as focal onset with rapid propagation versus multifocal/generalized epilepsy, thereby refining seizure classification and informing more tailored treatment plans. More accurate localization can reduce the need for extensive invasive monitoring, shorten time to surgery, and increase the likelihood of seizure freedom following resection [3]. At the same time, refined seizure classification would enable a more rational decision between pharmacological versus surgical management strategies.

4.7 | On Clinical Integration and Feasibility

Although the performance demonstrated by geometric eigenmodes is promising, successful clinical translation depends not only on accuracy, but also on interpretability and workflow compatibility. The output of the method, estimated source activation maps, can be visualized using standard cortical surface projections, similar to those already used in clinical neuroimaging such as CURRY. For localization of epileptogenic zones within a cohort of people with epilepsy, geometric eigenmodes offered superior recall compared to widely used inverse solutions, with no compromise in precision or other performance metrics [23, 68]. This suggests that geometric eigenmodes could supplement, rather than replace, current noninvasive imaging techniques like PET or SPECT by refining hypotheses about seizure onset zones before invasive studies. Compared to approaches requiring individual diffusion MRI and tractography for each patient, geometric eigenmodes offer a lower-burden alternative. The finding that subject-specific eigenmodes were not essential implies feasibility in a wider variety of clinical situations, though having individual T1 MRI remains preferable for a more accurate forward model. As presurgical evaluation becomes increasingly improved by computational models and non-invasive imaging [54, 79, 80], tools like the geometric eigenmode approach may serve as a valuable addition to the clinician's toolbox, bridging the gaps between observed clinical manifestations, patient brain structure, hidden functional seizure dynamics, and accurate patient prognosis. Future clinical validation would involve larger prospective cohorts, benchmarking against gold-standard outcomes such as Engel classification post-surgery, assessing real-time feasibility, and exploring integration with iEEG and surgical navigation platforms.

4.8 | On Limitations

In this work, several algorithm parameters were fixed as part of the experimental design and assumptions. The depth weighting, which adjusts the forward model, was not applied. As with most EEG source localization methods, the recovery of deep sources using structural eigenmodes is expected to be more sensitive to noise, and a systematic evaluation of deep and

subcortical sources remains a direction for future work. Dipoles were assumed to be fixed and oriented perpendicular to the cortical surface, but the orientation could have been loose. Care must be taken when considering loose orientations, as results can be misleading as discussed in Section S1.7. The choice of the β parameter for eigenmode weighting as a function of the eigenvalues (Equation (8)) was based on physical arguments, rather than optimization. Similarly, the steps involved in the construction of the connectome, such as spatial smoothing and thresholding, relied on expert judgement. Although all of these parameters can be adjusted and tuned in practice, extensive tuning of hyperparameters risks overfitting to a specific dataset and may compromise the generalizability of the methodology.

Another main limitation was the reliance on simulation as the source of truth for evaluation. While simulations provide valuable ground truth for assessing methodological performance, they inevitably simplify the complexity of real neural dynamics and are unlikely to capture the full range of noise and variability present in real-world data. Specifically, while the Epileptor model is considered state of the art and has a strong track record of reproducing many spatial and temporal features of epileptic dynamics at both microscale and macroscale levels [35, 52, 55], its canonical form captures only one of the twelve theoretically defined dynamical transitions associated with seizure activity [81]. Moreover, assumptions made during simulation design, such as source extent, timescales, and propagation dynamics, may introduce biases in favor of specific modelling approaches. For example, the reliance of the coupled neural mass model on the structural connectome may advantage the connectome eigenmode approach by construction. Nevertheless, while absolute accuracy in simulation often overestimates performance in real data, relative performance trends, such as the comparative ranking of methods or the impact of specific parameter adjustments, often generalize.

To address these concerns, we complemented the simulation-based evaluation with application to real patient data from individuals who underwent surgical resection. However, it's important to reiterate that from a clinical perspective, the localization of interictal spikes does not necessarily reflect the true epileptogenic zone, which may confound the evaluation and risks over-interpretation. This highlights the need for future work to systematically validate the approach in prospective studies across diverse patient populations, ideally incorporating multi-modal data such as fMRI or intracranial recordings to better assess clinical utility and confirm generalizability. Although simulations cannot substitute for clinical validation, in domains like source localization where a definitive ground truth is currently not available, they serve as a critical intermediary, helping to guide expectations, identify limitations, and narrow the space of viable methods prior to clinical deployment.

5 | Conclusion

Source localization is an important technique for improving the spatial accuracy of EEG and MEG measurements [5]. Improved algorithms will lead to an improved understanding of the brain, such as advances in our knowledge of consciousness [82], and has direct applications in the diagnosis and treatment of neurological disorders. This work combined the recent pivotal idea in computational neuroscience of structural eigenmodes to biologically constrain the optimization problem of source localization and found it to be highly effective in representing neurologically plausible signals in terms of its accuracy, computational efficiency, and ease of use. Furthermore, the presented approach showed promise in noninvasively analyzing the origins of ictal and interictal activities, which may one day drive improved outcomes for people with epilepsy.

Acknowledgements

The author would like to thank the Australian neuroimaging and computational neuroscience community for their encouragement and support, as well as the international friends met during travel in the Americas. This research was supported by The University of Melbourne's Research Computing Services, the Petascale Campus Initiative, and an Australian Government Research Training Program (RTP) Scholarship. This research was funded by the Australian Research Council (Discovery Project DP200102600).

Open access publishing facilitated by The University of Melbourne, as part of the Wiley - The University of Melbourne agreement via the Council of Australasian University Librarians.

Conflicts of Interest

The authors declare no conflicts of interest.

Data Availability Statement

All code for the source localization pipeline can be found at: https://github.com/Spokhim/sesl. All code should be easily compatible with current MNE-Python pipelines whether it is EEG or MEG. If there is enough interest, the author may look into a proper implementation into MNE-Python.

References

1. B. Ettore, "Global, Regional, and National Burden of Epilepsy, 1990–2016: A Systematic Analysis for the Global Burden of Disease Study 2016," *The Lancet Neurology* 18, no. 4 (April 2019): 357–375, https://www.ncbi.nlm.nih.gov/pmc/articles/PMC6416168/.

2. J. S. Duncan, G. P. Winston, M. J. Koepp, and S. Ourselin, "Brain Imaging in the Assessment for Epilepsy Surgery," *The Lancet Neurology* 15, no. 4 (April 2016): 420–433, https://www.sciencedirect.com/science/article/pii/S147444221500383X.

3. H. M. Khoo, J. A. Hall, F. Dubeau, et al., "Technical Aspects of SEEG and Its Interpretation in the Delineation of the Epileptogenic Zone," *Neurologia Medico-Chirurgica* 60, no. 12 (December 2020): 565–580, https://www.ncbi.nlm.nih.gov/pmc/articles/PMC7803703/.

4. P. L. Nunez and R. Srinivasan, *Electric Fields of the Brain* (Oxford University Press, January 2006), https://academic.oup.com/book/2998.

5. B. He, A. Sohrabpour, E. Brown, and Z. Liu, "Electrophysiological Source Imaging: A Noninvasive Window to Brain Dynamics," *Annual Review of Biomedical Engineering* 20, no. 1 (2018): 171–196, https://doi.org/10.1146/annurev-bioeng-062117-120853.

6. H. Hallez, B. Vanrumste, R. Grech, et al., "Review on Solving the Forward Problem in EEG Source Analysis," *Journal of NeuroEngineering and Rehabilitation* 4, no. 1 (November 2007): 46, https://doi.org/10.1186/1743-0003-4-46.

7. W. E. Kincses, C. Braun, S. Kaiser, and T. Elbert, "Modeling Extended Sources of Event-Related Potentials Using Anatomical and Physiological Constraints," *Human Brain Mapping* 8, no. 4 (1999): 182–193.

8. S. Haufe, R. Tomioka, T. Dickhaus, et al., "Large-Scale EEG/MEG Source Localization with Spatial Flexibility," *NeuroImage* 54, no. 2 (January 2011): 851–859, https://www.sciencedirect.com/science/article/pii/S1053811910011729.

9. J. C. Pang, K. M. Aquino, M. Oldehinkel, et al., "Geometric Constraints on Human Brain Function," *Nature* (May 2023): 1–9, https://www.nature.com/articles/S41586-023-06098-1.

10. R. M. Potash, W. F. Z. Yang, B. Winston, et al., "Investigating the Complex Cortical Dynamics of an Advanced Concentrative Absorption Meditation Called Jhanas (ACAM-J): A Geometric Eigenmode Analysis," *Cerebral Cortex* 35, no. 2 (February 2025): bhaf039, https://doi.org/10.1093/cercor/bhaf039.

11. A. Milloz, J. Vogel, A. Olsen, et al., "Multiscale Quantification of Hemispheric Asymmetry in Cortical Maps Using Geometric Eigenmodes," in *2025 IEEE 22nd International Symposium on Biomedical Imaging (ISBI)* (April 2025): 1–5, https://ieeexplore.ieee.org/abstract/document/10980761.

12. A. Boyes, P. E. Schwenn, Z. Y. Shan, et al., "Geometric Eigenmode Brain Fingerprinting and Its Longitudinal Associations with Adolescent Mental Health and Wellbeing," (August 2024), https://www.biorxiv.org/content/10.1101/2024.08.08.607260v1.

13. M. G. Preti and D. Van De Ville, "Decoupling of Brain Function from Structure Reveals Regional Behavioral Specialization in Humans," *Nature Communications* 10, no. 1 (October 2019): 4747, https://www.nature.com/articles/S41467-019-12765-7.

14. I. Rigoni, J. Rué Queralt, K. Glomb, et al., "Structure-Function Coupling Increases During Interictal Spikes in Temporal Lobe Epilepsy: A Graph Signal Processing Study," *Clinical Neurophysiology* 153 (September 2023): 1–10, https://www.sciencedirect.com/science/article/pii/S1388245723006429.

15. L. Sina Mansour, H. Behjat, D. V. De Ville, R. E. Smith, B. T. Yeo, and A. Zalesky, "Eigenmodes of the Brain: Revisiting Connectomics and Geometry," (April 2024), http://biorxiv.org/lookup/doi/10.1101/2024.04.16.589843.

16. J. Faskowitz, D. Moyer, D. A. Handwerker, et al., "Commentary on Pang et al. (2023) Nature," (July 2023), https://www.biorxiv.org/content/10.1101/2023.07.20.549785v1.

17. S. Hou, X. Liu, Y. Yu, and Q. Wang, "Functional Modal Feature Analysis Based on the Network Transition Dynamics of Epileptic Seizure," *Chaos, Solitons & Fractals* 197 (August 2025): 116500, https://www.sciencedirect.com/science/article/pii/S0960077925005132.

18. S. Hou, H. Wang, Y. Yu, X. Liu, and Q. Wang, "Identifying Dynamical Characteristics of Directed Functional Epilepsy Networks from Eigenmodes," *Science China Technological Sciences* 68, no. 5 (April 2025): 1520404, https://doi.org/10.1007/S11431-024-2828-0.

19. S. Wang, C. Wei, K. Lou, D. Gu, and Q. Liu, "Advancing EEG/MEG Source Imaging with Geometric-Informed Basis Functions," in *2024 46th Annual International Conference of the IEEE Engineering in Medicine and Biology Society (EMBC)* (July 2024): 1–4, https://ieeexplore.ieee.org/document/10782170/.

20. J. Rué-Queralt, H. Fluhr, S. Tourbier, et al., "Connectome Spectrum Electromagnetic Tomography: A Method to Reconstruct Electrical Brain Source Networks at High-Spatial Resolution," *Human Brain Mapping* 45, no. 5 (March 2024): e26638, https://www.ncbi.nlm.nih.gov/pmc/articles/PMC10960556/.

21. A. Giri, L. Kumar, N. Kurwale, and T. K. Gandhi, "Anatomical Harmonics Basis Based Brain Source Localization with Application to Epilepsy," *Scientific Reports* 12, no. 1 (July 2022): 11240, https://www.nature.com/articles/S41598-022-14500-7.

22. R. Sun, A. Sohrabpour, G. A. Worrell, and B. He, "Deep Neural Networks Constrained by Neural Mass Models Improve Electrophysiological Source Imaging of Spatiotemporal Brain Dynamics," *Proceedings of the National Academy of Sciences* 119, no. 31 (August 2022): e2201128119, https://www.pnas.org/doi/abs/10.1073/pnas.2201128119.

23. C. Plummer, S. J. Vogrin, W. P. Woods, M. A. Murphy, M. J. Cook, and D. T. J. Liley, "Interictal and Ictal Source Localization for Epilepsy Surgery Using High-Density EEG with MEG: A Prospective Long-Term Study," *Brain* 142, no. 4 (April 2019): 932–951, https://doi.org/10.1093/brain/awz015.

24. L. D. Cioppa, M. Tartaglione, A. Pascarella, and F. Pitolli, "Solution of the EEG Inverse Problem by Random Dipole Sampling," *Inverse Problems* 40, no. 2 (December 2023): 025006, https://dx.doi.org/10.1088/1361-6420/ad14a1.

25. Y. Petrov, "Harmony: EEG/MEG Linear Inverse Source Reconstruction in the Anatomical Basis of Spherical Harmonics," *PLOS ONE* 7, no. 10 (October 2012): e44439, https://journals.plos.org/plosone/article?id=10.1371/journal.pone.0044439.

26. J. Rong, R. Sun, B. Joseph, G. Worrell, and B. He, "Deep Learning-Based EEG Source Imaging Is Robust Under Varying Electrode Configurations," *Clinical Neurophysiology* (April 2025), https://www.sciencedirect.com/science/article/pii/S1388245725005693.

27. L. Hecker, R. Rupprecht, L. Tebartz Van Elst, and J. Kornmeier, "ConvDip: A Convolutional Neural Network for Better EEG Source Imaging," *Frontiers in Neuroscience* 15 (2021), https://www.frontiersin.org/articles/10.3389/fnins.2021.569918.

28. M. Morik, A. Hashemi, K.-R. Müller, S. Haufe, and S. Nakajima, "Enhancing Brain Source Reconstruction Through Physics-Informed 3D Neural Networks," (2024), https://arxiv.org/abs/2411.00143.

29. J. B. Burt, M. Demirtaş, W. J. Eckner, et al., "Hierarchy of Transcriptomic Specialization Across Human Cortex Captured by Structural Neuroimaging Topography," *Nature Neuroscience* 21, no. 9 (September 2018): 1251–1259, http://www.nature.com/articles/S41593-018-0195-0.

30. V. M. Eguíluz, D. R. Chialvo, G. A. Cecchi, M. Baliki, and A. V. Apkarian, "Scale-Free Brain Functional Networks," *Physical Review Letters* 94, no. 1 (January 2005): 018102, https://link.aps.org/doi/10.1103/PhysRevLett.94.018102.

31. S. B. Eickhoff, B. T. T. Yeo, and S. Genon, "Imaging-Based Parcellations of the Human Brain," *Nature Reviews Neuroscience* 19, no. 11 (November 2018): 672–686, https://www.nature.com/articles/S41583-018-0071-7.

32. K. B. Doelling and M. F. Assaneo, "Neural Oscillations Are a Start Toward Understanding Brain Activity Rather Than the End," *PLOS Biology* 19, no. 5 (May 2021): e3001234, https://journals.plos.org/plosbiology/article?id=10.1371/journal.pbio.3001234.

33. D. P. Koller, M. Schirner, and P. Ritter, "Human Connectome Topology Directs Cortical Traveling Waves and Shapes Frequency Gradients," *Nature Communications* 15, no. 1 (April 2024): 3570, https://www.nature.com/articles/S41467-024-47860-x.

34. P. H. Siu, E. Müller, V. Zerbi, K. Aquino, and B. D. Fulcher, "Extracting Dynamical Understanding from Neural-Mass Models of Mouse Cortex," *Frontiers in Computational Neuroscience* 16 (2022), https://www.frontiersin.org/articles/10.3389/fncom.2022.847336.

35. S. A. Moosavi, V. K. Jirsa, and W. Truccolo, "Critical Dynamics in the Spread of Focal Epileptic Seizures: Network Connectivity, Neural Excitability and Phase Transitions," *PLOS ONE* 17, no. 8 (August 2022): e0272902, https://journals.plos.org/plosone/article?id=10.1371/journal.pone.0272902.

36. Y. Zhao, D. B. Grayden, M. Boley, et al., "Cortical Stability and Chaos During Focal Seizures: Insights from Inference-Based Modeling," *Journal of Neural Engineering* 22, no. 3 (May 2025): 036021, https://doi.org/10.1088/1741-2552/add83f.

37. D. C. Van Essen, S. M. Smith, D. M. Barch, T. E. J. Behrens, E. Yacoub, and K. Ugurbil, "The WU-Minn Human Connectome Project: An Overview," *NeuroImage* 80 (October 2013): 62–79, https://www.sciencedirect.com/science/article/pii/S1053811913005351.

38. B. Fischl, "FreeSurfer," *NeuroImage* 62, no. 2 (August 2012): 774–781.

39. X. Yan, R. Kong, A. Xue, et al., "Homotopic Local-Global Parcellation of the Human Cerebral Cortex from Resting-State Functional Connec-

tivity," *NeuroImage* 273 (June 2023): 120010, https://linkinghub.elsevier.com/retrieve/pii/S1053811923001568.

40. M. F. Glasser, S. N. Sotiropoulos, J. A. Wilson, et al., "The Minimal Preprocessing Pipelines for the Human Connectome Project," *NeuroImage* 80 (October 2013): 105–124, https://linkinghub.elsevier.com/retrieve/pii/S1053811913005053.

41. S. Mansour L, Y. Tian, B. T. Yeo, V. Cropley, and A. Zalesky, "High-Resolution Connectomic Fingerprints: Mapping Neural Identity and Behavior," *NeuroImage* 229 (April 2021): 117695, https://linkinghub.elsevier.com/retrieve/pii/S1053811920311800.

42. S. Mansour L, M. A. Di Biase, R. E. Smith, A. Zalesky, and C. Seguin, "Connectomes for 40,000 UK Biobank Participants: A Multi-Modal, Multi-Scale Brain Network Resource," *NeuroImage* 283 (December 2023): 120407, https://www.sciencedirect.com/science/article/pii/S105381192300558X.

43. J.-D. Tournier, R. Smith, D. Raffelt, et al., "MRtrix3: A Fast, Flexible and Open Software Framework for Medical Image Processing and Visualisation," *NeuroImage* 202 (November 2019): 116137, https://linkinghub.elsevier.com/retrieve/pii/S1053811919307281.

44. B. Jeurissen, J.-D. Tournier, T. Dhollander, A. Connelly, and J. Sijbers, "Multi-Tissue Constrained Spherical Deconvolution for Improved Analysis of Multi-Shell Diffusion MRI Data," *NeuroImage* 103 (December 2014): 411–426, https://linkinghub.elsevier.com/retrieve/pii/S1053811914006442.

45. T. Dhollander, D. Raffelt, and A. Connelly, "Unsupervised 3-Tissue Response Function Estimation from Single-Shell or Multi-Shell Diffusion MR Data Without a Co-Registered T1 Image," in *ISMRM Workshop on Breaking the Barriers of Diffusion MRI*, vol. 5 (Lisbon, 2016).

46. J. D. Tournier, F. Calamante, A. Connelly, et al., "Improved Probabilistic Streamlines Tractography by 2nd Order Integration over Fibre Orientation Distributions," in *Proceedings of the International Society for Magnetic Resonance in Medicine*, vol. 1670 (Stockholm, 2010).

47. R. E. Smith, J.-D. Tournier, F. Calamante, and A. Connelly, "Anatomically-Constrained Tractography: Improved Diffusion MRI Streamlines Tractography Through Effective Use of Anatomical Information," *NeuroImage* 62, no. 3 (September 2012): 1924–1938, https://linkinghub.elsevier.com/retrieve/pii/S1053811912005824.

48. B. He, T. Musha, Y. Okamoto, S. Homma, Y. Nakajima, and T. Sato, "Electric Dipole Tracing in the Brain by Means of the Boundary Element Method and Its Accuracy," *IEEE Transactions on Biomedical Engineering* BME-34, no. 6 (June 1987): 406–414.

49. A. Gramfort, T. Papadopoulo, E. Olivi, and M. Clerc, "OpenMEEG: Open-Source Software for Quasistatic Bioelectromagnetics," *BioMedical Engineering OnLine* 9, no. 1 (September 2010): 45, https://doi.org/10.1186/1475-925X-9-45.

50. A. Gramfort, M. Luessi, E. Larson, et al., "MNE Software for Processing MEG and EEG Data," *NeuroImage* 86 (February 2014): 446–460, https://www.sciencedirect.com/science/article/pii/S1053811913010501.

51. K. Sekihara and S. S. Nagarajan, *Electromagnetic Brain Imaging: A Bayesian Perspective* (Springer International Publishing, 2015), https://link.springer.com/10.1007/978-3-319-14947-9.

52. V. K. Jirsa, W. C. Stacey, P. P. Quilichini, A. I. Ivanov, and C. Bernard, "On the Nature of Seizure Dynamics," *Brain* 137, no. 8 (August 2014): 2210–2230, https://doi.org/10.1093/brain/awu133.

53. V. K. Jirsa, T. Proix, D. Perdikis, et al., "The Virtual Epileptic Patient: Individualized Whole-Brain Models of Epilepsy Spread," *NeuroImage* 145 (January 2017): 377–388, https://www.sciencedirect.com/science/article/pii/S1053811916300891.

54. V. Jirsa, H. Wang, P. Triebkorn, et al., "Personalised Virtual Brain Models in Epilepsy," *The Lancet Neurology* (March 2023), https://www.sciencedirect.com/science/article/pii/S147444222300008X.

55. H. E. Wang, M. Woodman, P. Triebkorn, et al., "Delineating Epileptogenic Networks Using Brain Imaging Data and Personalized Modeling in Drug-Resistant Epilepsy," *Science Translational Medicine* 15, no. 680 (January 2023): eabp8982, https://www.science.org/doi/10.1126/scitranslmed.abp8982.

56. T. Proix, V. K. Jirsa, F. Bartolomei, M. Guye, and W. Truccolo, "Predicting the Spatiotemporal Diversity of Seizure Propagation and Termination in Human Focal Epilepsy," *Nature Communications* 9, no. 1 (March 2018): 1088, https://www.nature.com/articles/S41467-018-02973-y.

57. P. Sanz-Leon, S. A. Knock, A. Spiegler, and V. K. Jirsa, "Mathematical Framework for Large-Scale Brain Network Modeling in The Virtual Brain," *NeuroImage* 111 (May 2015): 385–430, https://linkinghub.elsevier.com/retrieve/pii/S1053811915000051.

58. P. Sanz Leon, S. A. Knock, M. M. Woodman, et al., "The Virtual Brain: A Simulator of Primate Brain Network Dynamics," *Frontiers in Neuroinformatics* 7 (2013), http://journal.frontiersin.org/article/10.3389/fninf.2013.00010/abstract.

59. K. E. Houssaini, C. Bernard, and V. K. Jirsa, "The Epileptor Model: A Systematic Mathematical Analysis Linked to the Dynamics of Seizures, Refractory Status Epilepticus, and Depolarization Block," *eNeuro* 7, no. 2 (March 2020), https://www.eneuro.org/content/7/2/ENEURO.0485-18.2019.

60. N. Otsu, "A Threshold Selection Method from Gray-Level Histograms," *IEEE Transactions on Systems, Man, and Cybernetics* 9, no. 1 (January 1979): 23–27.

61. R. Sun, A. Sohrabpour, B. Joseph, G. Worrell, and B. He, "Seizure Sources Can Be Imaged from Scalp EEG by Means of Biophysically Constrained Deep Neural Networks," *Advanced Science* 11, no. 47 (2024): 2405246, https://onlinelibrary.wiley.com/doi/abs/10.1002/advs.202405246.

62. N. C. Koussis, J. C. Pang, R. Phogat, et al., "Generation of Surrogate Brain Maps Preserving Spatial Autocorrelation Through Random Rotation of Geometric Eigenmodes," *Imaging Neuroscience* 3 (July 2025): IMAG.a.71, https://doi.org/10.1162/IMAG.a.71.

63. J. Kaipio and E. Somersalo, "Statistical Inverse Problems: Discretization, Model Reduction and Inverse Crimes," *Journal of Computational and Applied Mathematics* 198, no. 2 (January 2007): 493–504, https://www.sciencedirect.com/science/article/pii/S0377042705007296.

64. J. J. Crofts, M. Forrester, S. Coombes, and R. D. O'Dea, "Structure-Function Clustering in Weighted Brain Networks," *Scientific Reports* 12, no. 1 (October 2022): 16793, https://www.nature.com/articles/S41598-022-19994-9.

65. C.-H. Yeh, D. K. Jones, X. Liang, M. Descoteaux, and A. Connelly, "Mapping Structural Connectivity Using Diffusion MRI: Challenges and Opportunities," *Journal of Magnetic Resonance Imaging* 53, no. 6 (2021): 1666–1682, https://onlinelibrary.wiley.com/doi/abs/10.1002/jmri.27188.

66. P. Nakkiran, G. Kaplun, Y. Bansal, T. Yang, B. Barak, and I. Sutskever, "Deep Double Descent," (January 2020), https://openai.com/index/deep-double-descent/.

67. J. W. Rocks and P. Mehta, "Memorizing Without Overfitting: Bias, Variance, and Interpolation in Overparameterized Models," *Physical Review Research* 4, no. 1 (March 2022): 013201, https://link.aps.org/doi/10.1103/PhysRevResearch.4.013201.

68. P. Sharma, M. Seeck, and S. Beniczky, "Accuracy of Interictal and Ictal Electric and Magnetic Source Imaging: A Systematic Review and Meta-Analysis," *Frontiers in Neurology* 10 (2019), https://www.frontiersin.org/articles/10.3389/fneur.2019.01250.

69. P. A. Robinson, C. J. Rennie, J. J. Wright, H. Bahramali, E. Gordon, and D. L. Rowe, "Prediction of Electroencephalographic Spectra from Neurophysiology," *Physical Review E: Statistical, Nonlinear, and Soft Matter Physics* 63, no. 2 Pt 1 (February 2001): 021903.

70. M. P. van den Heuvel and H. E. Hulshoff Pol, "Exploring the Brain Network: A Review on Resting-State fMRI Functional Connectivity," *European Neuropsychopharmacology* 20, no. 8 (August 2010): 519–534, https://www.sciencedirect.com/science/article/pii/S0924977X10000684.

71. N. C. Gabay and P. A. Robinson, "Cortical Geometry as a Determinant of Brain Activity Eigenmodes: Neural Field Analysis," *Physical Review E* 96, no. 3 (September 2017): 032413, https://link.aps.org/doi/10.1103/PhysRevE.96.032413.

72. B. Belaoucha and T. Papadopoulo, "Structural Connectivity to Reconstruct Brain Activation and Effective Connectivity Between Brain Regions," *Journal of Neural Engineering* 17, no. 3 (June 2020): 035006, https://dx.doi.org/10.1088/1741-2552/ab8b2b.

73. S. J. Prince, *Understanding Deep Learning* (The MIT Press, 2023), http://udlbook.com.

74. L. E. Sainburg, D. J. Englot, and V. L. Morgan, "The Impact of Resective Epilepsy Surgery on the Brain Network: Evidence from Post-Surgical Imaging," *Brain* 148, no. 6 (June 2025): 1866–1875, https://doi.org/10.1093/brain/awaf026.

75. J. Zou, H. Chen, X. Chen, et al., "Noninvasive Closed-Loop Acoustic Brain-Computer Interface for Seizure Control," *Theranostics* 14, no. 15 (September 2024): 5965–5981, https://www.thno.org/v14p5965.htm.

76. E. D. Schlafly, F. A. Marshall, E. M. Merricks, et al., "Multiple Sources of Fast Traveling Waves During Human Seizures: Resolving a Controversy," *Journal of Neuroscience* 42, no. 36 (September 2022): 6966–6982, https://www.jneurosci.org/content/42/36/6966.

77. E. H. Smith, J.-Y. Liou, T. S. Davis, et al., "The Ictal Wavefront Is the Spatiotemporal Source of Discharges During Spontaneous Human Seizures," *Nature Communications* 7, no. 1 (March 2016): 11098, https://www.nature.com/articles/ncommS11098.

78. C. A. Schevon, S. Tobochnik, T. Eissa, et al., "Multiscale Recordings Reveal the Dynamic Spatial Structure of Human Seizures," *Neurobiology of Disease* 127 (July 2019): 303–311, https://www.sciencedirect.com/science/article/pii/S0969996119300038.

79. M. Cao, S. J. Vogrin, A. D. H. Peterson, W. Woods, M. J. Cook, and C. Plummer, "Dynamical Network Models from EEG and MEG for Epilepsy Surgery—A Quantitative Approach," *Frontiers in Neurology* 13 (2022), https://www.frontiersin.org/articles/10.3389/fneur.2022.837893.

80. M. Cao, D. Galvis, S. J. Vogrin, et al., "Virtual Intracranial EEG Signals Reconstructed from MEG with Potential for Epilepsy Surgery," *Nature Communications* 13, no. 1 (February 2022): 994, https://www.nature.com/articles/S41467-022-28640-x.

81. M. L. Saggio, D. Crisp, J. M. Scott, et al., "A Taxonomy of Seizure Dynamotypes," *eLife* 9 (July 2020): e55632, https://elifesciences.org/articles/55632.

82. Y. Zhao, N. Tsuchiya, M. Boley, et al., "Cortical Connectivity, Local Dynamics and Stability Correlates of Global Conscious States," *Communications Biology* 8, no. 1 (September 2025): 1391, https://www.nature.com/articles/S42003-025-08782-6.

Supporting Information

Additional supporting information can be found online in the Supporting Information section.

Supporting File: advs74887-sup-0001-SuppMat.pdf.